ABSTRACT

WILLIAMS, ZACHARY WILLIS. Insights into the Mechanical Thickness: A Structural Analysis of Ridge Belt. (Under the direction of Dr. Paul K. Byrne).

Despite Venus showing no evidence of a global system of tectonic deformation, a variety of tectonic landforms across Venus suggests a complex and active geologic history that is not fully understood. One of the most ubiquitous tectonic landforms identified are linear to arcuate, positive-relief systems of shortening structures widely distributed within Venus' lowlands, termed ridge belts. Although these landforms have been recognized for some time, the relatively recent availability of regional topography at resolutions greater than the Magellan altimetry dataset enables the morphology and structure of ridge belts to be studied in finer detail. Additionally, the improved vertical resolution of these data allows for construction of computational models with which to estimate the mechanical thickness of the lithosphere.

Detailed morphometric data (strike, width, and relief) and cross-sectional profiles were collected for a globally distributed set of ridge belts. Once such data were acquired, observable tectonic structures—faults and folds— were mapped within a subset of those selected ridge belts. Identification of individual structures within ridge belts was based on comparative morphology with shortening structures on Earth. Cross-sectional profiles and relief values were then used to acquire local estimates for the mechanical thickness of the lithosphere. These estimates were derived using two separate modeling approaches. The first approach was inverse modeling of the lithosphere's flexural response to the ridge belt, evidenced by flexural signatures in topography proximal to these ridge belts. The second was forward-modeling of elastic dislocation along underlying fault geometries, curve-fitting surface deformation resulting from motion along a modeled fault plane to observed topography. The fault penetration depth of the theoretical fault

plane then represents a minimum possible depth to the brittle-ductile transition and therefore thickness of the mechanical lithosphere.

Morphometric analysis of the belts returns relatively low-relief values, with none in excess of 1 km, despite a wide range of width values in the 10s of km, indicating that low, positive relief is the most consistent morphological parameter. Cross-sectional profiles across these belts display fore- and back-limb morphology consistent with thrust-fault related landforms. We interpret tectonic structures within the ridge belts as predominately thrust faults and related anticlinal folds, the majority of which strike roughly parallel to the long axis of the host ridge belt. Results from morphological analysis and structural interpretation leads to the view that ridge belts are complex systems of thrust fault duplexes, in contrast to shortening structures on other worlds that are often morphologically more simple.

Estimates for mechanical lithospheric thickness from downflexing of the surrounding lithosphere in response to ridge belt loading returned values between 1.4 and 25.3 km. results from elastic dislocation forward-modeling returned mechanical lithospheric thickness values between 15.3 and 23.4 km. The uniformly low relief values for these ridges, together with the flexural and elastic dislocation model results, agree with previous studies that suggests the elastic lithosphere in the Venus lowlands is mechanically thin in comparison to values on Earth due to elevated surface temperatures.

Insights into the Mechanical Lithosphere of Venus: A Structural Analysis of Ridge Belts

by
Zachary Willis Williams

A thesis submitted to the Graduate Faculty of
North Carolina State University
in partial fulfillment of the
requirements for the degree of
Master of Science

Marine, Earth, and Atmospheric Sciences

Raleigh, North Carolina
2021

APPROVED BY:

_____	_____
Dr. Paul K. Byrne Committee Chair	Dr. Delwayne Bohnenstiehl
_____	
Dr. Karl W. Wegmann	

DEDICATION

This thesis is dedicated to my family, without whom the completion of this work would not have been possible. To my father, who instilled a lifelong interest in the sciences. To my mother, who fostered both my academic and life pursuits. To my sister, for her constant and continued support.

"We are all in the gutter, but some of us are looking at the stars." –Oscar Wilde

BIOGRAPHY

My interest in planetary science began well before the advent of my academic career. In a sense, I never grew out of my "dinosaur phase" that most young boys go through. My borderline obsession with ancient life always led to me wondering what was there before the dinosaurs? Of course, this line of reasoning does not stop there, what about before life on this planet, and what about other planets? Asking these grand questions at a young age inevitably set in motion a lifelong desire to explore, and a desire to become a planetary scientist as I would later discover.

Throughout my academic career and young life, I was met with bountiful opportunity, most of which I failed miserably. I was a good student, but never top of my class, I played sports but was never a formidable athlete. But I was there and tried, nonetheless, and I credit this ability to try and fail with getting me as far as I have. In high school I began to focus my juvenile interest in the sciences into a potential career by making a legitimate attempt in a mandatory science fair. This effort netted me second place in the field of physics for the entire state of Virginia and impassioned my drive to become a scientist. The state science fair was held at Old Dominion University in Norfolk, VA, which would in turn become where I attended my undergraduate education.

It was at ODU that I truly honed my skills as a scientist. Within a successful Ocean, Earth, and Atmospheric Science program, I finally got all the answers I once asked as a kid, and inevitably open the door to countless more. And after finding my success at ODU, I pushed on to finally pursue my lifelong dream of exploration by enrolling in the planetary science program at North Carolina State University. In this thesis, you will find the culmination of my lifelong interests as a single work. And in reading this, I hope you will find the same fascination and passion for planetary exploration that I have found my whole life.

ACKNOWLEDGMENTS

I would like to first acknowledge the sources of funding that prevented me from taking on crippling debt. The NC State Graduate Student Support plan for the first year and a half, on which I learned the skills and fulfillment of being an educator. And the NASA Solar System Workings (ROSES C.3) for providing funding through the conclusion of the research contained within this thesis (grant # 80NSSC20K0466). Next, I would like to acknowledge the mentorship I received at NC State. Chiefly Dr. Paul Byrne, who took me as a student and helped me to apply my lifelong interest into concrete results and skills. My committee members, Drs. Karl Wegmann and DelWayne Bohnenstiehl, who served as both academic mentors and people I could entrust to get me on the right path. I would also like to acknowledge the invaluable guidance of my fellow planetary research group members, specifically Rachel Atkins, Mallory Kinczyk, and Corbin Kling. On top of getting their PhDs, they took ample time out of their schedules to ensure my success. Finally, I would like to thank my close friends and family. I would like to acknowledge my mom, dad, and sister for helping me figure out how to navigate life as a student. And I would like to recognize my close friends: Scott, Connor, Nate, Alex, Pollard, Hunter, and so many others for their encouragement and understand during this process.

TABLE OF CONTENTS

LIST OF TABLES

LIST OF FIGURES

1. Introduction

Although Venus does not today show any evidence of a globally interconnected system of tectonic deformation, such as Earth's network of tectonic plates, global radar mapping of Venus has revealed extensive crustal deformation that attests to the planet's active geologic history (Young & Hansen, 2005; Hansen, 2018). One of the most prominent surface features observed are bands of radar-bright lineations termed ridge belts, first identified from the Venera 15 and 16 radar images (Barsukov et al., 1986; Frank and Head, 1990). These landforms appear widely distributed throughout otherwise relatively undeformed plains units as arcuate to linear systems up to hundreds of kilometers in length and tens of kilometers wide (**Fig. 1**) (Frank and Head, 1990; Squyres et al., 1992; Solomon et al., 1992; Ivanov and Head, 2013). Radar altimetry data collected during the NASA Magellan mission showed that the observed deformation in synthetic aperture radar (SAR) surveys accompanies broad topographic rises on the order of hundreds of meters high. These findings led some to a community assumption that ridge belts represent surface expressions of crustal shortening accommodated by a combination of thrust faults and folds (Solomon et al., 1992; Suppe and Connors, 1992; Squyres et al., 1992). However, the altimetry data collected by the Magellan mission has resolutions of ~10–20 kilometers per pixel (km/px). Furthermore, although these data can accurately resolve the morphological properties of large landforms that are hundreds of kilometers in scale, smaller structures, such as ridge belts, are poorly resolved.

To improve the quality of topographic data available for Venus, Herrick et al. (2012) performed stereo feature matching of ~20% of the planet's surface, for which there was multi-angle radar imaging by the Magellan mission. This effort resulted in a considerable improvement

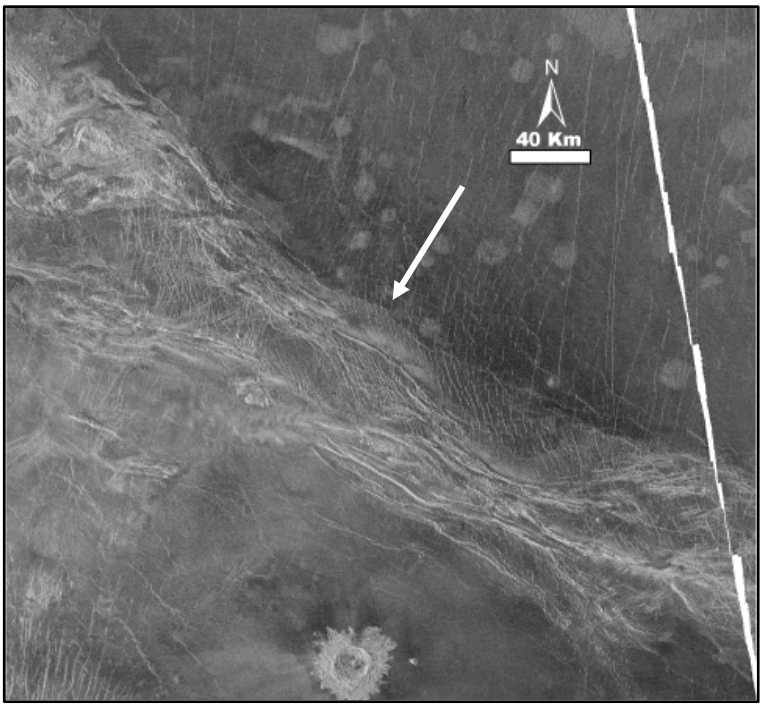

Figure 1. An example of a ridge belt, indicated by the white arrow, used in this study centered about 46 S°, 107 W° as seen within the left-look Magellan synthetic aperture radar imagery.

to the resolution of available topographic data, of 1–2 km/px (Herrick et al., 2012)—enabling the structure and morphology of ridge belts to be studied in finer detail. Preliminary studies of ridge belts utilizing these new data showed an asymmetric cross-sectional profile flanked by short and long wavelength depressions, which cannot be resolved with the Magellan altimetry data (Balcerski and Byrne, 2018a; b). Given the scale of surface deformation relative to these improved digital elevation models (DEM), ridge belts present an opportunity to investigate the structural histories and properties of the crust that have been previously unresolvable.

Here, we utilized these higher-resolution DEMs to gain insight into the Venusian crust's structure and evolution by characterizing the tectonic deformation of ridge belts. We acquired detailed morphometric data for a globally distributed set of ridge belts. Once such data were

acquired, we mapped observable tectonic structures—faults and folds—within a subset of those selected ridge belts and, together with morphometry results, developed a more robust characterization of ridge belt structure. These findings were then used to guide computational approaches to estimate the local effective lithospheric thickness at several ridge belts.

Studies of the rheological behavior of a basaltic crust under the temperature and pressure conditions at the Venus surface have predicted a relatively thin effective elastic lithosphere compared to Earth (Buck, 1992; Suppe & Connors, 1992; Ghail, 2015). Thinner lithospheres, and subsequent thinner brittle portions of the crust, allow for a greater range of long-wavelength tectonic phenomena, including the lithosphere's flexural response to crustal loading (e.g., Klimczak et al. 2019). Indeed, the asynchronous development of short-wavelength deformation (faulting within the ridge belt representing local tectonics) and longer-wavelength regional isostatic response to crustal loading on Venus has been previously noted (Zuber & Parmentier, 1990; Young & Hansen, 2005). We thus employed analytical solutions to match the observed deflection of the lithosphere in response to the ridge belt's mass loading for determining the effective elastic thickness of the lithosphere for the low-lying plains regions in which the ridge belts are located.

We observe that the morphology and structure of ridge belts are consistent with the deformation of a relatively thin mechanical lithosphere. We interpret ridge belts to result from complex systems of contractional fault duplexes and conjugate thrust faulting. Modeling the depth to the brittle-ductile transition (BDT) by curve fitting both the flexural response to crustal loading and surface deformation from faulting results in mechanical lithospheric thickness estimates of less than 24 kilometers (compared to 25–40 km depths on Earth).

1.1. Data

For morphological and structural analyses, we utilized global Magellan synthetic aperture radar full-resolution radar map (SAR FMAP) 100-meter-per-pixel (m/px) left- and right-look mosaics. For elevation data, we used the stereo-derived DEMs produced by Herrick et al. (2012), which offer ~20% global coverage at ~1–2 km/px.

1.2. Ridge Belt Selection

We conducted a global survey in the ArcGIS environment to identify ridge belts based on morphological descriptions from existing studies (Frank and Head, 1990; Solomon et al., 1992; Basilevsky and Head, 2003; McGill and Campbell, 2006; Ivanov and Head, 2011). Using both the left- and right-look Magellan SAR FMAP mosaics, the surface of Venus was parsed into 10°

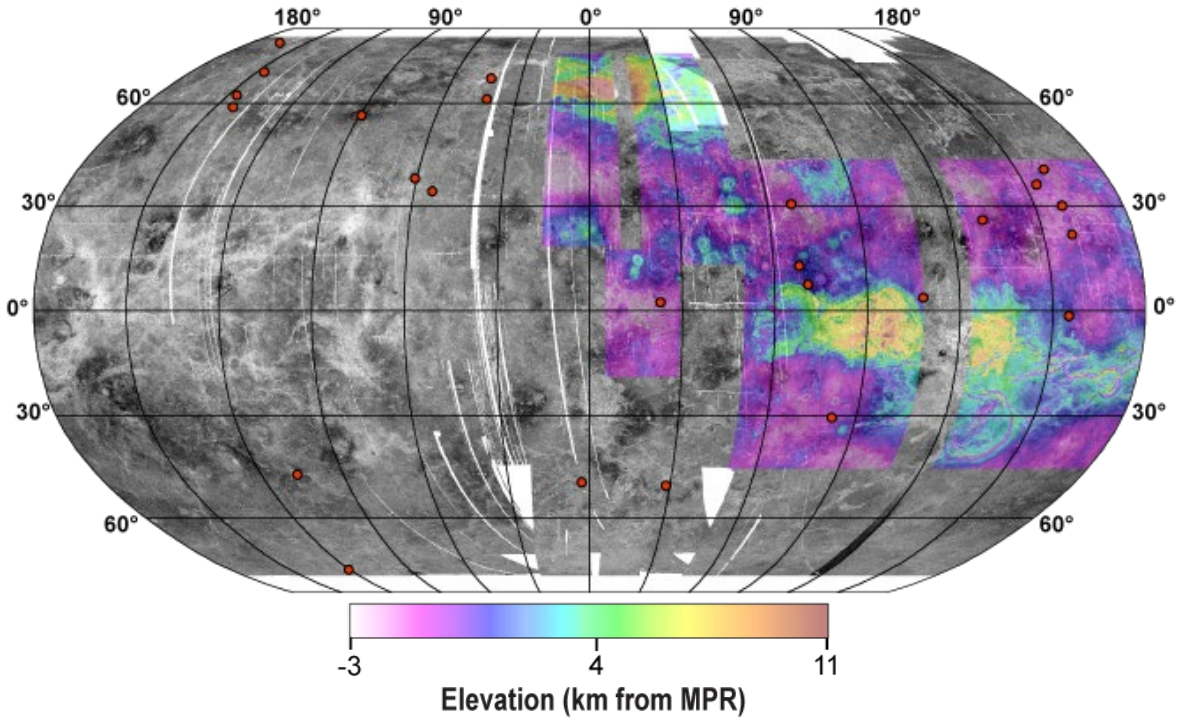

Figure 2. Robinson Projection of the Magellan left-look SAR survey (greyscale background) overlaid by the Herrick et al. (2012), DEMs (colored to indicate elevation in kilometers from mean planetary radius). The location of ridge belts selected for this study are shown by the red points.

× 10° bins and systematically examined for ridge belt candidates. View scale was varied during this examination to find ridge belts of various sizes. This initial survey yielded 398 discrete candidate landforms that we downselected to 25 for further analysis; the final candidates were selected based on having well-preserved morphology (i.e., not bisected by craters, buried by volcanism, or destroyed by subsequent tectonism). Of these 25 structures, 12 are within the higher-resolution DEM coverage (**Fig. 2**). We then centered an azimuthal equidistant projected coordinate system upon each of the 25 ridge belts to minimize distortions in our subsequent analyses.

2. Ridge Morphometry

Outlines of the selected ridge belts were manually traced and recorded within ArcGIS. We developed a Python routine to automatically record each landform's strike from the mapped outline and determine the centerline. These centerlines are interpreted to represent the general approximation of anticlinal fold axes of the ridge belts, from which fold-limb slope profiles orthogonal to the centerline were drawn. Width measurements orthogonal to the ridge axis at the point of collection, representing the distance across strike to opposing boundaries of the landform, were also collected at ~20 km intervals along each structure. The collection of multiple width measurements at different points along every ridge belt allowed us to characterize variance in width for individual belts, as well as for the variance between all study belts. Twenty profiles were drawn, orthogonal to the ridge axis at the point of collection, for the 13 ridge belts within higher-resolution data coverage. The length of these profiles was three times that of the ridge belt's width to include the surrounding plains material in which the ridge belts are situated.

Because of the compression and transmission of data to Earth from the Magellan spacecraft, and post-processing of those data (Ford, 1993; Herrick et al. 2012), artifacts exist

within the higher-resolution DEMs. These artifacts result in high-amplitude and high-frequency spatial variations (e.g., errant spikes and dips with no corresponding surface expression on radar image data) within the profiles that are not topological, and which hinder interpretation of the acquired topographic profiles. Cross-sectional profiles were filtered to remove these artifacts, with careful consideration given to the method used to minimize the addition of false signals or remove relevant data. We used a fast-Fourier transform (FFT), treating each profile as a waveform to determine the relevant topographic frequencies to filter the data (Ojeda and Whitman, 2002). Because the profiles have a finite length and are not repeated, we applied a Hanning window and zero-padded the data before applying the FFT (Ojeda and Whitman, 2002). Each profile was then run through a low-pass filter scaled with the highest amplitude signal set as the threshold value. Results show a minimal loss in each profile's shape and dimensions, yet an efficient removal of processing artifacts (**Fig. 3**).

Relief was calculated for the 12 ridge belts covered by the Herrick et al. (2012) DEMs using the elevation pixel values within the traced outline to create a hypsometric curve. This method was employed to maximize the higher-resolution DEMs' utility, by incorporating as many pixel values as possible rather than downsampling the data into profiles. By calculating relief as the weighted mean to a hypsometric curve, we could more accurately determine relief values but minimize the impact of processing artifacts without excluding data. A similar method was used by Ivanov and Head (2011) when looking at the ridged plains regions on Venus en masse; here, we applied this method to individual ridge belts.

2.1. Morphometry Results

The location (latitude and longitude), azimuth, width (maximum, minimum, and standard deviation), and ridge belt relief are listed in **Table 1**. The average width of the 25 ridge belts is

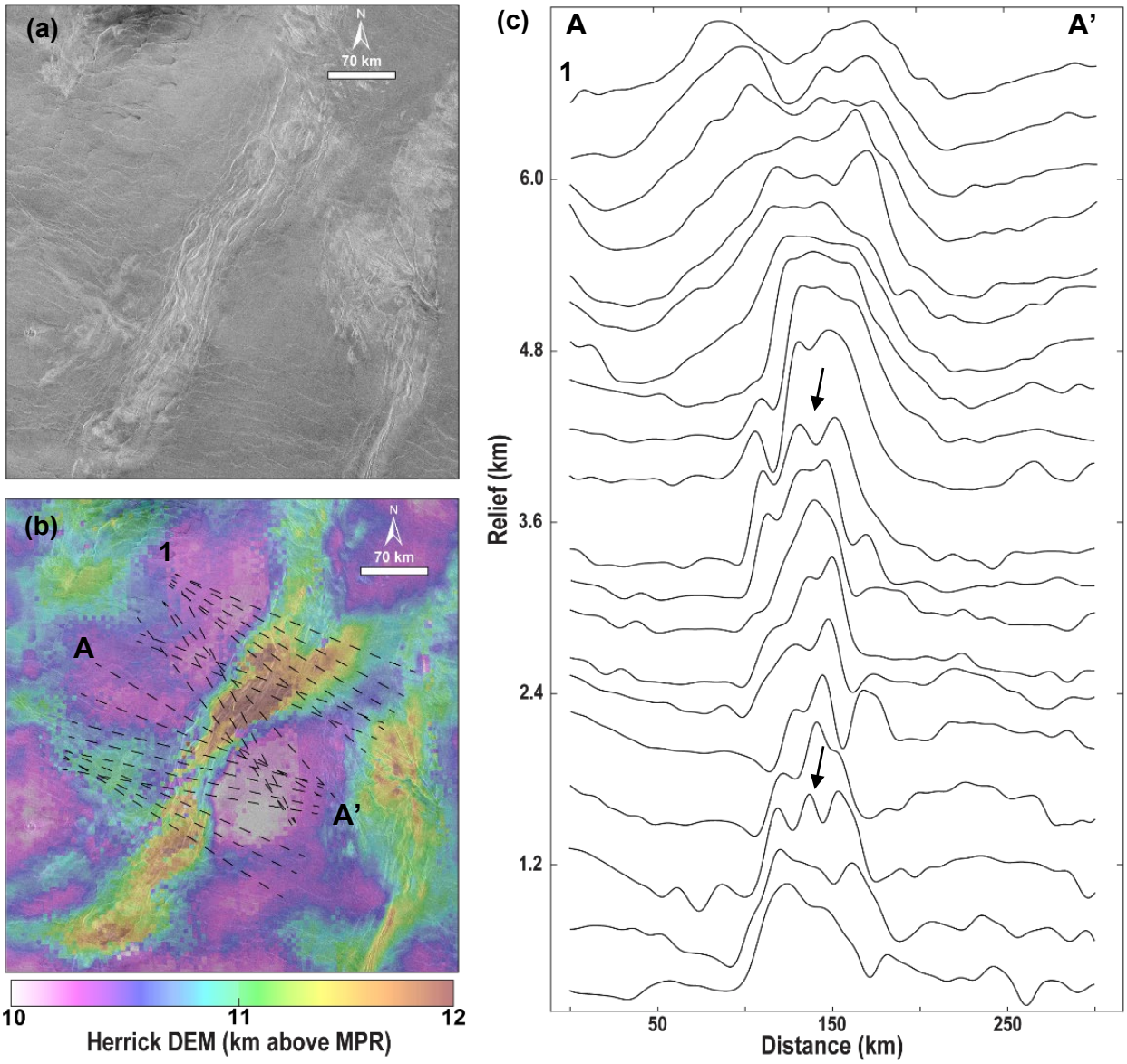

Figure 3. Example of a ridge belt seen with (**a**) left-look Magellan radar image data, and with the Herrick DEM data (**b**); corresponding topographic profiles are shown in (**c**). Dashed black lines show the locations of the profiles and their orientation, as noted by the A and A' symbology. Profiles progress from top to bottom (**c**) as northeast to southwest on the map (**b**).

75 km (median = 63 km), with a maximum of 207 km and a minimum of 9 km. The standard deviation of width measurements within each ridge belt ranged from 4 to 39 km, with an average of 15 km.

Table 1. Morphological properties of ridge belts included in this study. Latitude, longitude, width mean, max, min, standard deviation and strike were collected using both the left- and right-look Magellan SAR surveys. Values for relief are given for those ridge belts within the higher-resolution DEM. Population statistics for Latitude and Longitude are not relevant for analysis. The mean strike value reported here represents the vector mean, with the resultant length given by the decimal in parathesis.

ID	Latitude	Longitude	Width Mean (km)	Width Max (km)	Width Min (km)	Width STD (km)	Strike (degrees)	Relief (m)
RB 1	69.94	-146.46	109	207	64	38	141	
RB 2	37.861	-61.244	100	121	75	14	50	
RB 3	34.18	-54.2	123	176	79	33	131	
RB 4	30.81	66.84	31	52	9	14	41	640
RB 5	21.97	157.79	83	108	64	15	37	640
RB 6	13.2	67.47	30	44	17	6	120	380
RB 7	12.77	67.26	24	33	18	5	130	330
RB 8	2.73	21.9	116	150	104	11	73	510
RB 9	7.98	69.46	26	38	13	7	127	830
RB 10	-41.19	20.68	45	65	30	9	141	
RB 11	26	129.2	52	65	43	6	101	440
RB 12	-29.94	80.13	36	48	31	4	158	370
RE 13	-5.58	162.24	51	64	34	8	127	680
RB 14	-78.6	-123.52	65	87	42	15	46	
RB 15	-49.44	27.32	42	59	32	7	0	
RB 16	-45.91	-106.8	71	115	38	24	123	
RB 17	-48.33	-6.73	127	202	62	37	74	
RB 18	68.85	-43.39	178	199	152	12	28	
RB 19	63.18	6.42	92	146	45	28	14	
RB 20	80.2	-163.64	145	167	122	13	173	
RB 21	61.34	-42.91	46	69	29	14	147	
RB 22	56.43	-89.66	93	110	57	16	0	
RB 23	30.184	157.39	57	79	40	13	31	790
RB 24	40.453	157.907	62	96	42	16	15	660
RB 25	36.259	152.365	63	77	43	10	8	440
Mean	N/A	N/A	75	103	51	15	84 (0.57)	560
Max	N/A	N/A	178	207	152	39	N/A	830
Min	N/A	N/A	24	33	9	4	N/A	330
Median	N/A	N/A	63	87	43	14	N/A	570

For the 12 ridges within the coverage of the Herrick et al. DEMs, we found an average relief value of 559 m, a median value of 572 m, and maximum and minimum values of 830 m and 332 m, respectively. Relief values are uniformly low—less than 1 km—despite these belts having widths of 9 to 207 km (and correspondingly high standard deviations). Thus, low topographic relief is the most consistent morphological parameter of the ridge belt ensemble.

Cross-sectional profiles commonly display a shape consistent with an asymmetric fold, wherein there is an observable difference in fore- and back-limb morphology (**Fig. 3, Appendix A1-2**). A cross-sectional morphology with this geometry is expected within fault-displacement-gradient folding arising from orthogonal crustal shortening (Wickham, 1995; Byrne, 2018; Klimczak et al., 2018). The orientation of the fore- and back-limbs commonly diverge (i.e., fold asymmetry switches) along strike for profiles that display such asymmetry. We interpret this finding to indicate vergence switching along the belt, a phenomenon expected from shortening structures of the horizontal length scale of ridge belts (i.e., several hundred kilometers) within a generally basaltic lithology. Superposed upon the overall fold morphology are shorter-wavelength ridges and troughs along the profile's apex (as shown by the black arrows in **Fig. 3**). We interpret these smaller-scale topographic to represent anticlinal folding within the ridge belt. Flanking the ridge belts are shallow (~300 m) depressions interpreted as the lithosphere's flexural response to mass loading by ridge belts.

3. Fault Mapping

Radar-bright lineations are interpreted as alterations in surface angle to the incident radar beam, in the case of ridge belts due to tectonic deformation (Ford, 1993; Ford, 1994). A persistent challenge of fault mapping without elevation data that can resolve the throw of individual faults is the determination of the fault dip direction, as identification of the hanging

and footwalls based on relative relief differences is the most common approach for remotely sensed fault mapping. Even with the improved Herrick DEMs, fault mapping predominantly requires the use of SAR surveys, at a horizontal resolution of ~100 m/px, sufficient to at least detect major alterations of surface angle due to faulting. Determination of the dip direction of individual faults within ridge belts is, however, important to accurately characterizing the nature of these landforms. We therefore developed a method to determine dip direction of the inferred faulting by examining both the fault trace morphology and radar backscatter.

When looking at fault morphology, shallow dipping thrust faults form sinuous and arcuate traces (Davis et al., 2012). Along the fault trace, the horizontal displacement reaches a maximum at a point along the trace and approaches zero at the tips, producing a characteristic curvature in map view (Davis et al., 2012). The apex of curvature must then be oriented in the direction of tectonic transport, with the fault tips oriented in the down-dip direction. Linear fault traces were commonly seen throughout radar images of ridge belts, which were interpreted as denoting either smaller-scale strike-slip or normal faulting to (Section 4.1). We note that sinuous fault trace morphology is not exclusive to thrust faults, and therefore requires fault morphology to be supplemented with individual fault interaction with SAR surveys to more accurately designate fault type.

Backscatter, the property collected by SAR, results from the radar beam interacting with surface roughness at a scale greater than the beam wavelength (Ford, 1993; Ford, 1994). Variation in backscatter is a function of the interaction between the radar beams and the target, primarily influenced by the surface roughness at scales less than the radar wavelength, dielectric constant, and incidence angle (which in turn is a function of topography) (Ford, 1993; Ford, 1994). Assuming similar surface mineralogy and erosional rate across the ridge belts, and thus

constant dielectric constant and surface roughness, respectively, the variation in backscatter is a function of incidence angle. The Magellan SAR surveys operated at 25° off-nadir; therefore, the steeper the surface angle, the brighter the backscatter coefficient (Ford et al., 1994). Indeed, small alterations in surface angle produce large backscatter changes for slopes below 20° (Ford, 1994). For ridge belts with both left- and right-look survey coverage and oriented approximately orthogonally to the radar look-direction, radar-brightness differences are observed along fault traces between surveys. This observation establishes the orientations of the landforms we interpret as antiforms atop thrust faults (i.e., hanging-wall anticlines), from which the dip direction of the thrust faults are derived.

With this combination of morphology and backscatter, we mapped individual tectonic structures within six of the selected ridge belts to create digital maps within ArcGIS. These six were selected based on an orientation orthogonal to the radar look directions and coverage by both left- and right-look SAR data. Four of these ridge belts were within the Herrick DEM coverage. Mapping of observable fault traces within the SAR FMAPs was done at a 1:200,000 view scale.

3.1. Structural Analysis

Interpretation of the complex structure within ridge belts first required discretizing individual fault populations, determined by fault type and orientation. In contrast to thrust faulting within ridge belts, which are identifiable by a combination of trace morphology and backscatter signal within stereo-imaging SAR, linear fault traces can reasonably correspond to either normal or strike-slip faulting. As mentioned in Section 4, it is difficult to determine any lateral offset within the Magellan SAR surveys, as the speckle noise within SAR imagery inhibits the recognition of offsets at the scale of observed faulting. The absence of resolvable

lateral offsets along linear fault traces, of course, does not preclude the existence of such offsets. We attempted to distinguish between normal or strike-slip faulting for these linear traces by determining if these fractures are strain compatible based on relative orientation with the observed thrust faults for which the dip direction could be inferred. Linear fault populations will be referenced as strike-slip or normal based on their relative orientation with thrust fault populations for the remainder of this paper.

After identifying the fault type, faulting populations were further discretized based on their orientation, with a suite of faults of similar type and orientation taken to indicate deformation resulting from a single deformation sequence. We observed that thrust fault traces typically display antithetic dip directions, which were used as a first-order approximation for defining separate populations. We then calculated each population's vector means, with the resultant length of the vectors used to quantify the distribution of fault orientation within each population (Kutil, 2012). A group of faults with a resultant length of 0.9 was considered a single population, with a lower value indicating the presence of multiple fault populations within that sample. In that instance, the population was further discretized until the 0.9 threshold value was met.

For each fault population identified, the cumulative length was calculated and compared between populations to determine if a dominant dip direction is present within each ridge belt. Dominant dip-directions that are found are taken to indicate the direction of tectonic transport of the entire ridge belt. At a 1:200,000 view scale, small-scale but numerous fault traces are almost certainly present but unresolvable with the Magellan data. Using cumulative length over fault count, we effectively normalized the fault populations to each fault's size and removed the impact of unresolvable faults.

Lateral spacing between thrust faults, which we took to correspond to fold spacing (discussed in more detail in Section 4.2), was measured within each ridge belt. Within large-scale shortening structures on Earth, the deformation style of fault-displacement-gradient folds can be better understood by examining the spatial relationships and geometry of observable folds (Suppe and Connors, 1992; Wickham, 1995). For this study, we focused on the spacing and width of folds as a proxy for the homogeneity of mechanical properties of the crustal shortening responsible for ridge belt formation. Consistency of fault (and corresponding fold) spacing within a ridge belt can be used as a first- order proxy for estimating the distribution of slip and the variation in dip angle along the major fault planes in a given belt.

3.2. Structural Results

Previous studies (e.g., McGill and Campbell, 2006; Ivanov and Head, 2011; 2013) suggested that ridge belts represent relatively recent tectonic activity, deforming older geological units but appearing to remain largely unembayed by subsequent lava flows post-dating ridge belt formation. Those ridge belts in this study thus represent the upper bound for the timing of deformation, with only one example showing flow margins appearing to follow (and thus postdate) major folds in the northernmost section (RB 15 seen in **Figure 4**).

It is common for anticlinal folds and antethtic fault pairs to form in association with imbricated thrust faults (**Fig 5, Appendix B1-3**). Indeed, our results show that mapped thrust fault traces occur in antithetic pairs throughout all the ridge belts included in this study (**Table 2**), agreeing with those earlier observations of cross-sectional morphology that suggest anticlinal folding within the studied ridge belts. Thrust faulting is observed to be the dominant deformation style within ridge belts with cumulative lengths an order of magnitude greater than that of any other population of structures we interpret as normal or strike-slip faults (**Table 2**). It is

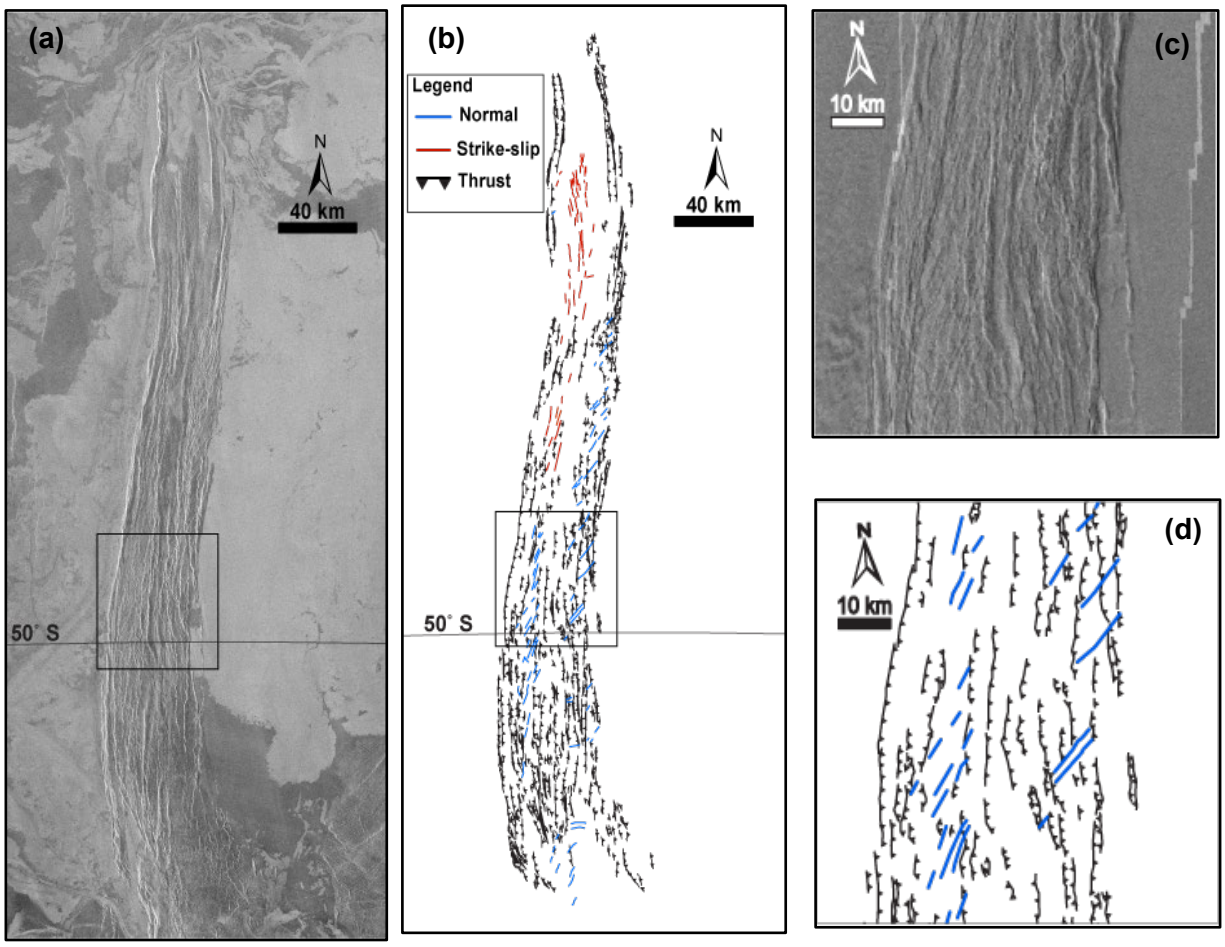

Figure 4. An exemplar ridge belt (RB 15) shown with (**a**) left-look SAR imagery (**b**) and our structural interpretation. Interpreted normal faults are shown in blue and thrust faults are in black, with teeth indicating the inferred down-dip direction. Folds and faults observed within the left- and right-look SAR (with right-look inverted) show a closer view of the tectonic fabric clearly visible with Magellan data (**c**), and apparent within our structural map (**d**). The black insets in (a) and (b) show the position of the close-up shown in (d). All maps are within a projected coordinate system centered about the ridge belt.

important to note that cumulative length of fault populations is used solely for comparative analysis within each individual ridge belt and is not valid for strain estimates. Additionally, displacement–length scaling relations for Venus faults have not been accurately established (Schultz et al., 2006). Finally, and of note, the comparison of cumulative length between thrust

fault populations within each belt yielded a direction of tectonic transport consistent with that suggested by fore- and back-limb morphology seen within the topographic profiles in the four ridge belts within the Herrick DEM that displayed such asymmetry (**Table 2**).

Localized groups of normal faults, offset in an en echelon manner, are interpreted as a response to localized extensional strain within some areas of the ridge belts. In some cases, we find localized suites of thrust faults offset in an en echelon manner, which form structures that, in map view, resemble restraining bends (**Fig. 6d**). Fault populations striking ~30° relative to thrust fault populations are taken to represent conjugate strike-slip faulting, that is strain compatible with the maximum compressive stress indicated by the observed thrust faults (**Fig 4d, Appendix B2**). Fault populations with linear traces along the outermost lateral extent of the ridge belts are taken to represent strike-slip splay faults that distributes lateral displacement across horse-tail structures (**Fig 6b**). Each of these populations represents the accommodation of transpressional shear strain, highlighting an oblique component to the dominantly orthogonal crustal shortening

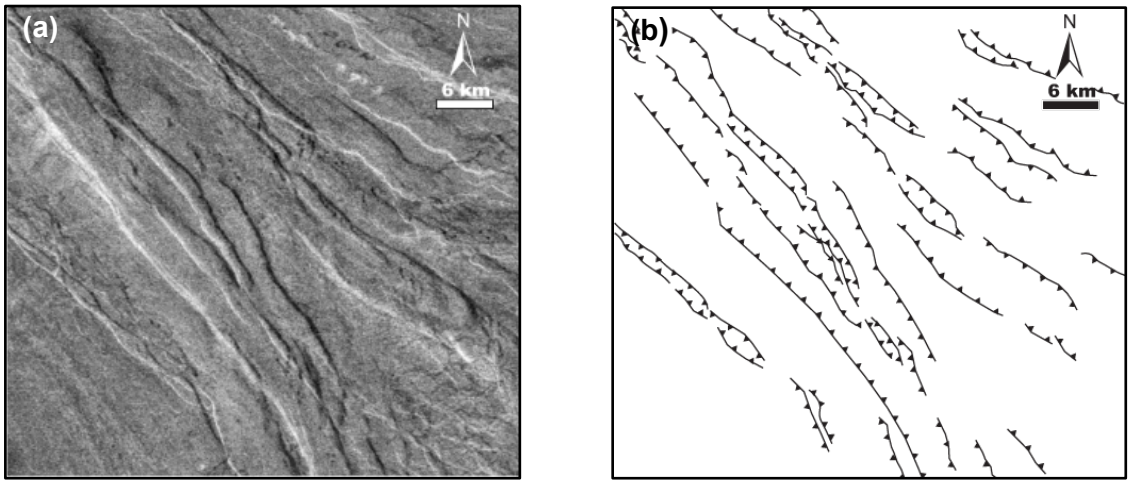

Figure 5. (**a**) Folds observed within left- and right-look SAR (with right-look inverted) at 1:200,000 view scale. (**b**) Structural map of faults; teeth indicate inferred down-dip fault direction. The pattern of antithetic thrust faults seen in this figure are common throughout the ridge belts analyzed in this study.

Table 2. Results of structural analysis for six ridge belts. Fault populations identified within each ridge belt are designated by their fault type with corresponding parameters. Parameters shown here include the dip direction, within thrust fault populations for which it can be derived, cumulative length (in km), spacing between antithetic thrust fault populations (in km) and the corresponding standard deviation of these values, and the lateral spacing between nearest neighbors within a single thrust fault population (in km) with the corresponding standard deviation.

ID	Morph.	Vector Mean (RL)	Dip	Length (km)	Antithetic Spacing (km)	Antithetic Spacing STD (km)	Pop. Spacing (km)	Pop. Spacing STD (km)
RB 6	Thrust	117 (0.94)	NE	541	$5.26^{(+1.05/-0.85)}$	0.5	$4.20^{(+0.57/-0.63)}$	0.3
	Thrust	306 (0.95)	SW	813				
RB 7	Thrust	125 (0.97)	NE	528	$4.71^{(+0.95/-0.81)}$	0.44	$2.71^{(+0.56/-0.46)}$	0.26
	Thrust	314 (0.96)	SW	473				
RB 10	Thrust	143 (0.96)	NE	3279	$2.84^{(+0.20/-0.19)}$	0.1	$2.63^{(+0.45/-0.34)}$	0.2
	Thrust	327 (0.97)	SW	2582				
	Thrust	38 (0.97)	NW	365				
	Thrust	201 (0.96)	SE	131				
	Thrust	132 (0.96)	NE	283				
	Thrust	343 (0.95)	SW	169				
	Strike-Slip	144 (0.90)	-	648				
RB 13	Thrust	322 (0.97)	NE	1061	N/A	N/A	N/A	N/A
	Thrust	137 (0.96)	SW	675				
	Normal	58 (0.98)	-	3458				
RB 14	Thrust	22 (0.96)	NW	1468	N/A	N/A	N/A	N/A
	Thrust	208 (0.96)	SE	146*				
	Strike-Slip	10 (0.98)	-	257				
	Normal	27 (0.99)	-	138				
	Strike-Slip	166 (0.97)	-	784				
RB 15	Thrust	181 (0.98)	E	2262	$3.0^{(+0.2/-0.1)}$	0.2	$3.1^{(+0.4/-0.2)}$	0.14
	Thrust	5 (0.99)	W	797				
	Strike-Slip	31 (0.98)	-	380				
	Normal	8 (0.99)	-	275				

Note. RB 14 features some distortion within the right-look SAR, limiting the observation of surface slope alterations from that look direction. Superscripts within the spacing columns represent 95% confidence intervals within the bootstrapping protocols.

that characterizes ridge belts. Lastly, normal fault populations were identified along the ridge axes of several ridge belts in this study. We interpret these extensional structures to represent the ridge's gravitational collapse based on a similar orientation with thrust faulting and occurrence upon the apex of the ridge axis.

The analysis of fold spacing yields two distinct findings: (**1**) fold length and spacing are generally uniform with relatively low variability, reflected by the standard deviation compared to the mean for antithetic and intrapopulation spacing of RB 10 and RB 15 (**Table 2)**, and (**2**) ridge belts with statistically different means between fold spacing and wavelength with higher variability seen in RB 6 and RB 7 (**Table 2)**. The mean and standard deviation of these values result from bootstrapping measurements (n = 5000), assuming that we acquired a representative sample population of fold spacing measurements across each ridge belt. The observed differences in fold spacing between ridge belts suggest that they do not represent a singular shortening style, and that faulting between ridge belts does not manifest in a uniform manner.

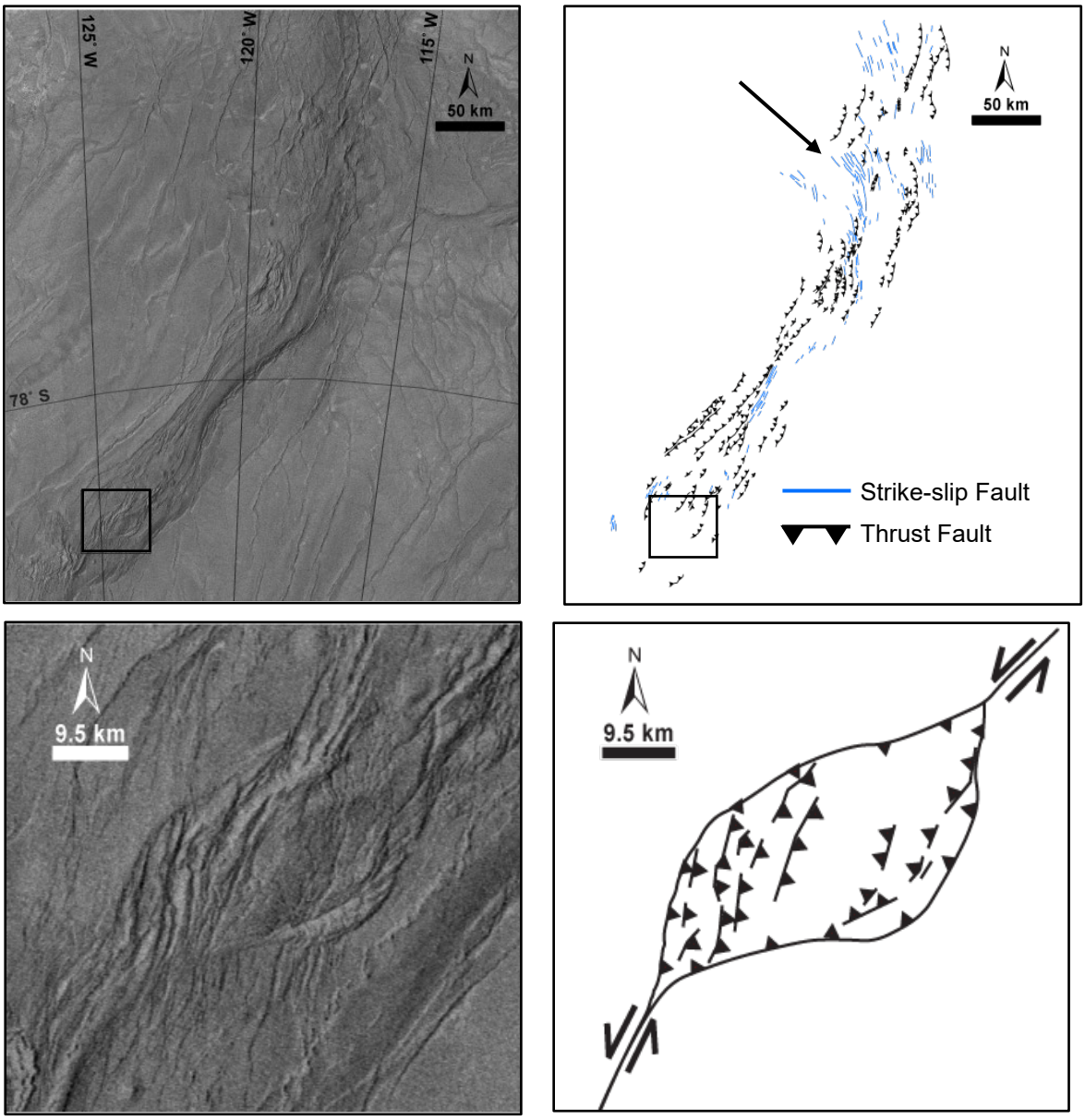

Figure. 6. A ridge belt centered about 78° S, 123° W that is (**a**) dominated by thrust faulting with linear fault population along the ridge axis and horse-tail structures along the northern tip (**b**) (shown by the black arrow). Black boxes give the location of an example of a structure morphologically consistent with a restraining bend, observed within right-look SAR at 1:200,000 view scale and (**c**) structural interpretation as a sinistral restraining bend, indicative of transpressional strain (**d**).

4. Lithospheric Flexure Models

On geological timescales, the rigid lithosphere behaves elastically atop the upper mantle that behaves as a viscous fluid, allowing the lithosphere to flex in response to vertically applied stress and reach a point of isostatic equilibrium. In the crustal shortening indicated by our structural analysis, the lithosphere thickens as more crust is accumulated during ridge belt

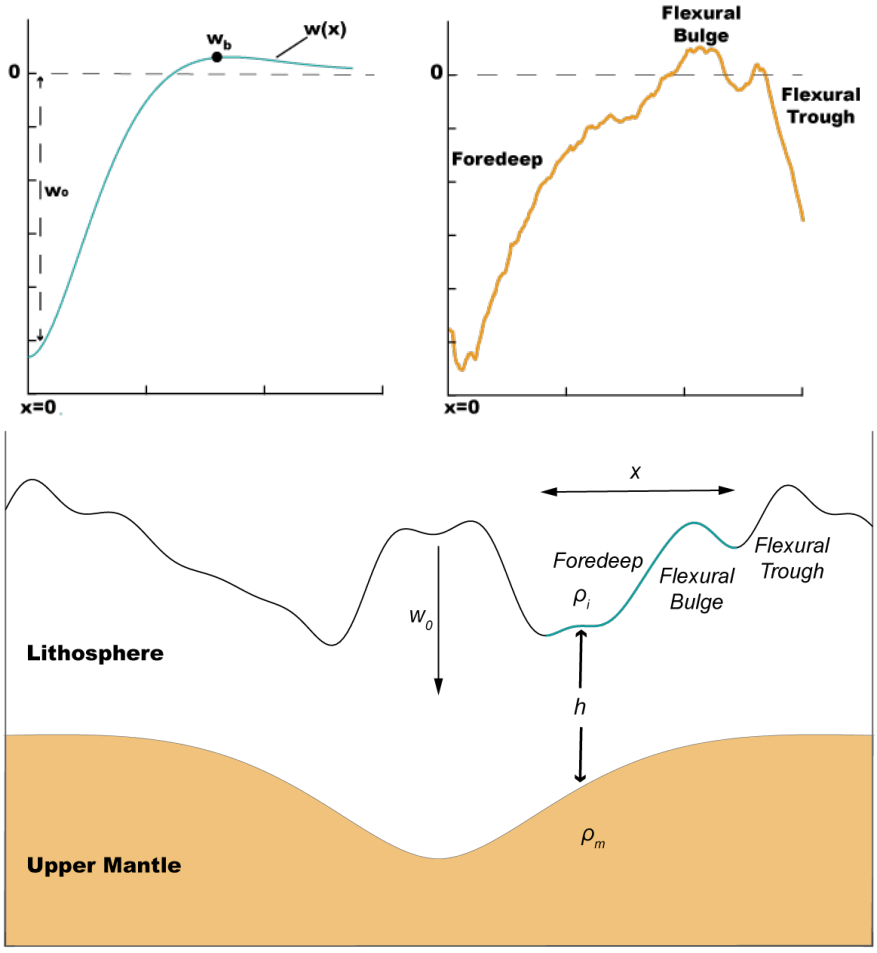

Figure 7. A schematic representation of lithospheric flexure in response to a line-load (**top left**) and (**b**) an example of an observed profile exhibiting the same morphology (**top-right**). A theoretical model for an observed profile and the lithospheric response to the ridge belt (not to scale). The flexural signals shown in the top figure are added here in context including the appropriate variables used in our calculations. The teal segment represents the model domain.

formation. The resulting concentration of crustal material results in an increased mass, representing a line-load on the lithosphere that then deforms to accommodate that load. This phenomenon is mechanically similar to the deflection of the oceanic lithosphere in response to loading by seamount chains. The wavelength and amplitude of the flexural response are dependent on the material properties of the lithosphere, and principally its rigidity, a function of its mechanical thickness.

Of the 13 ridge belts for which sets of profiles were drawn, six were identified that display clear evidence for having down-flexed their supporting lithosphere (**Fig. 7**). From this observation, an analytical approach was applied to test the lithospheric response to an individual ridge, treating each as a line load by curve fitting modeled profiles to the observed deflection and solving for the elastic lithospheric thickness. The analysis was performed on several profiles along each selected ridge belt. The solution to the topographic response to a line load (represented as a point load on a one-dimensional profile), *w*, is given by the dampened sinusoidal function (Fowler, 2012):

$$w = w_0 e^{-\frac{x}{a}}\left(\cos\left(\frac{x}{a}\right) + \sin\left(\frac{x}{a}\right)\right), \qquad [1]$$

where w_0 is the maximum amplitude of flexure along the breadth of the profile, *x*, with respect to the flexural parameter, *a*, given by the relation:

$$a = \sqrt[4]{\frac{4D}{(\rho_m - \rho_i)g}}, \qquad [2]$$

where *D* is the flexural rigidity, $\rho_m - \rho_i$ is the difference between mantle and atmospheric density, and *g* is the acceleration due to gravity. Flexural rigidity is given by:

$$D = \frac{E}{12(1-v^2)}h^3, \qquad [3]$$

where *E* is Young's modulus, *v* is Poisson's ratio, and *h* is the depth of the elastic lithosphere.

Values for Young's modulus and Poisson's ratio for anhydrous basalt, and density contrast across the lithosphere, were taken from previous lithospheric flexure studies on Venus (Schultz, 1993; Anderson and Smrekar, 2006; O'Rourke and Smrekar, 2018). The depth of the elastic lithosphere was determined with a least-squares optimization of a root-mean-squared cost function for the set of equations using a simplex method, with h and w_0 as two of the free parameters. The minimization function was built in Matlab and run with 100,000 iterations.

4.1. Lithospheric Flexure results

Solutions to the lithospheric response to crustal loading were derived for all profiles for which a flexural trough and bulge were identified. Results for analytical solutions under a 0.2 root-mean-squared error (RMSE), normalized by the range on the z-axis, were considered adequate fits and reported here in this study, which we regarded to be an appropriate approximation of the observed deflection (**Table 3**). Solutions to multiple profiles along each ridge belt included in this survey revealed a range of values, for which we report the average. We find absolute effective lithospheric values ranging from 1.4 to 25.3 km, with the averages for profiles within a single ridge ranging from 5.7 to 14.5 km.

Table 3. Lithospheric flexure analytical solutions. This tale presents all solutions below a 0.2 RMSE, normalized by the range of the z-axis. Depth values represent the effective elastic thickness for the lithosphere.

ID	Profile	Depth (km)	Mean (km)	RMSE
RB 6	5	1.4	5.7	0.09
RB 6	13	9.8		0.17
RB 7	18	4.7	5.9	0.16
RB 7	4	4.0		0.03
RB 7	5	2.5		0.05
RB 7	6	3.3		0.2
RB 7	11	10.4		0.1
RB 7	10	10.7		0.11
RB 8	1	12.5	14.5	0.06
RB 8	2	8.3		0.13
RB 8	10	22.0		0.09
RB 8	13	8.2		0.05
RB 8	14	8.3		0.15
RB 8	15	11.0		0.17
RB 8	17	25.3		0.1
RB 8	18	20.5		0.11
RB 9	4	11.1	5.7	0.04
RB 9	9	2.9		0.05
RB 9	10	6.9		0.07
RB 9	11	2.5		0.05
RB 9	13	1.4		0.08
RB 9	14	12.2		0.14
RB 9	18	2.6		0.09
RB 13	2	7.2	8.8	0.04
RB 13	3	5.3		0.08
RB 13	6	5.0		0.06
RB 13	9	17.8		0.07
RB 23	19	7.7	9.1	0.05
RB 23	1	9.3		0.06
RB 23	2	9.8		0.07
RB 23	6	7.9		0.06
RB 23	7	6.4		0.09
RB 23	18	15.2		0.06
RB 23	19	7.2		0.05

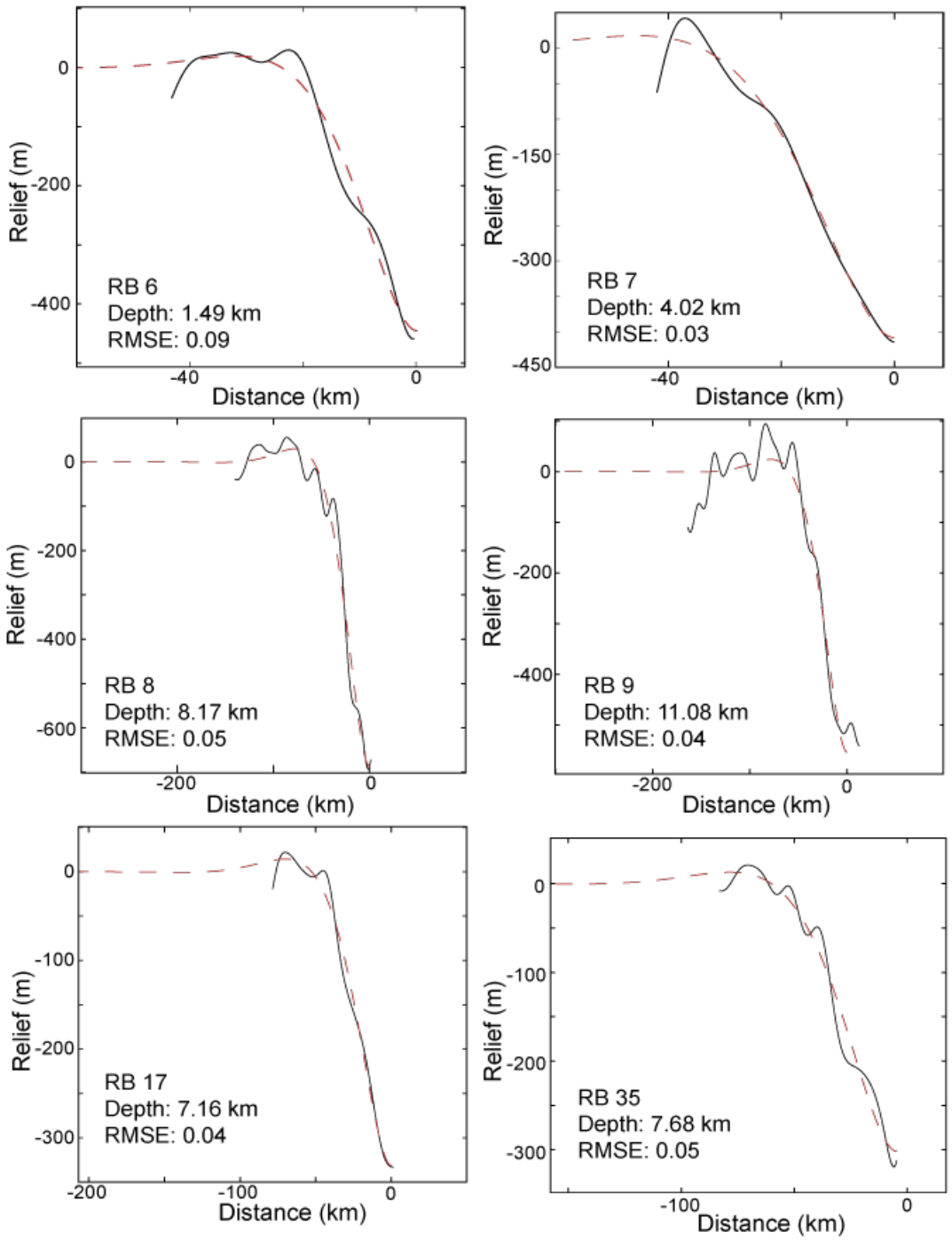

Figure 8. Curve fitting of modeled topographic response to lithospheric line loads (red dotted line) compared with observed topography (black). These plots constitute the best fit across every ridge belt within this study. Ridge profile IDs and values for effective lithospheric thickness and normalized RMSE values are shown in each plot's bottom left.

5. Elastic Dislocation Modeling

The relationship between the morphology of folds and the geometry of underlying faults has long been investigated and used to develop kinematic models for crustal shortening (Suppe, 1983, Shultz & Waters, 2001; Wickham 1995, Correder et al., 2005). Numerical modeling of fault behavior and resulting surface deformation has been used to extend topographic data to capture the faulting environment and mechanical properties of the crust for a variety of shortening structures (Williams et al., 1994; Shultz and Watters, 2001; Byrne et al., 2015; Klimczak et al., 2018). Shear failure—that is, faulting—is restricted to rock that behaves in a brittle manner, and which occurs only in the upper crust, below which primarily increasing temperature controls the transition to thermally activated plastic deformation mechanics. Therefore, the maximum penetration depth of faulting provides a minimum value for the depth to the brittle-ductile transition zone. By forward modeling a range of possible fault configurations using the Coulomb 3.3 elastic dislocation software, we reproduced best fits to modeled surface displacement versus observed surface topography. Model solutions thereby place constraints on the maximum depth extent for major fault planes responsible for ridge belt formation, and an estimate of the BDT depth on Venus (Shultz, 1993; Schultz and Watters, 2001; Anderson and Smrekar, 2006; James et al., 2013).

Guided by our structural analysis results, we estimated the geometry and penetration depth of the major thrust fault planes beneath four ridge belts using the Coulomb 3.3 elastic dislocation software within Matlab. The modeling of fault-driven elastic dislocation is a continuum mechanics problem. Coulomb 3.3 is a finite element model. Therefore, fault configuration files needed to be carefully constructed to simulate continuum processes. The framework of our hypothetical fault construction was as follows.

1. Three-dimensional planar fractures represented faults within Coulomb within an infinite isotropic elastic half-space;
2. Faulting was exclusively modeled as elastic behavior, independent of temperature and pressure fluctuations with depth;
3. Motion along the fault was time-invariant, occurring as a single event;
4. The dip, slip amount, and position of the fault within model space was user defined;
5. Fault planes that changed dip angle or slip with depth were constructed as linked segments with differing parameters.

We created a suite of user-defined fault geometries that iterated through a parameter space of possible slip amounts, dip angles, and vertical and horizontal coordinates for a given belt's underlying fault plane. Input files were iteratively produced by looping through the user-defined suite for each parameter value, as shown in **Table 4**.

These values were limited to earlier iterations of model testing that produced surface deformation at a similar scale to the real-world ridge belt profiles. The parameter space was refined by removing incompatible combinations that are not physically possible. Such unrealistic

Table 4. Parameter values and increments for used in the construction of elastic dislocation model inputs

Parameter	Range of Values	Increment
Dip Angle, θ	10-80°	2°
Penetration Depth, Z_{Max}	4-40 km	1 km
Burial Depth, Z_{Min}	0 or 1 km	N/A
Slip Amount, D	8-30 km	2 km

configurations were defined as fault planes longer than 200 km along the X-axis, thus beyond the model grid's scope, and a total slip along the fault plane that is greater than the length of the fault plane. Informed by the complex structure inferred to be present within ridge belts discussed in Section 3.2, we considered three separate fault geometries. Our modeled solutions include fault-bend folds, fault-propagation folds, and listric thrust faults as possible geometries responsible for the ridge belt antiforms.

The structural complexity seen in our study ridge belts indicates that these systems are likely the surface manifestations of successive deformation events with generally consistent stress vectors through time. Because fault-bend folding is closely related to reactivated folding on preexisting fault planes (Suppe, 1983, Suppe & Connors, 1992), incorporating this fold geometry into our analysis was warranted. This consideration is also supported by morphological findings of consistent spacing of anticlines and similarly dipping fore- and backlimbs in some of the collected cross-sectional profiles. Fault-bend folds are simulated in the model space by creating three fault segments: an upper and lower detachment, connected by a ramp. The slip amount was consistent across all three planes and was user-defined, along with each plane's position and the dip angle of the ramp (**Fig. 9a**). Because surface deformation from fault-bend folding is characterized by shallow-dipping fold limbs that reflect the ramp's dip angle (Hughes & Shaw, 2014), we limited the model space for these fault dip angle inputs to under 10°, resulting in a total of 8,592 fault-bend fold configurations.

One of the most widely documented fault-related-folding styles on Earth, surface displacement from fault-propagation folding, occurs in response to an upward-propagating fault tip (Hughes et al., 2014). We incorporated fault-propagation fold geometry within our model space due to the observed similarity between idealized kinematic models of fault-propagation

folds and topographic profiles. Surface deformation from fault-propagation folding is represented by profiles that display differences in fold limb angle (i.e., cross-sectional asymmetry), with the steeper forelimb corresponding to the direction of tectonic transport suggested by the thrust fault dip angle at the surface (**Figure. 9b**). The observed fold accommodates differential displacement along the fault, with a maximum displacement at depth tapering to zero at the fault tip (Mitra, 1986; Hughes et al., 2014). Fault-propagation model inputs were constructed to simulate the time-dependent displacement in a single event by tapering the displacement along the fault. This configuration was achieved by having ten segments of equal fault dip angle, θ, and slip amount, D, that root to the same depth, Z_{Max}, yet taper out at defined intervals, Z_{min}, thereby simulating a fault-propagation fault via the cumulative displacement from overlapping segments (**Fig. 9c**). Because we assumed this fault geometry roots to the BDT, this type of model fault bottomed out at a horizontal detachment with an equivalent slip to the base of the fault plane. This fault geometry also had the desired effect of removing excessive negative topography in the hinterland in the modelled ridge belts. We iterated through a total of 13,024 fault-propagation fold model configurations within our forward model.

Large thrust faults that form over a detachment layer may exhibit a listric geometry (Buchanan & McClay, 1991; Peterson et al., 2020). It is also common for listric thrust faults to form within a mechanically thin layer that roots to a detachment zone (Chapple, 1978; Davis et al., 2012). Given that we constructed fault configurations under the assumption that these faults root to a relatively shallow detachment, we deemed it pertinent to include the listric thrust fault geometry in this analysis. As for the fault-propagation folding, displacement along the fault plane segments tapered to zero at the fault tip, with a maximum displacement at depth, and

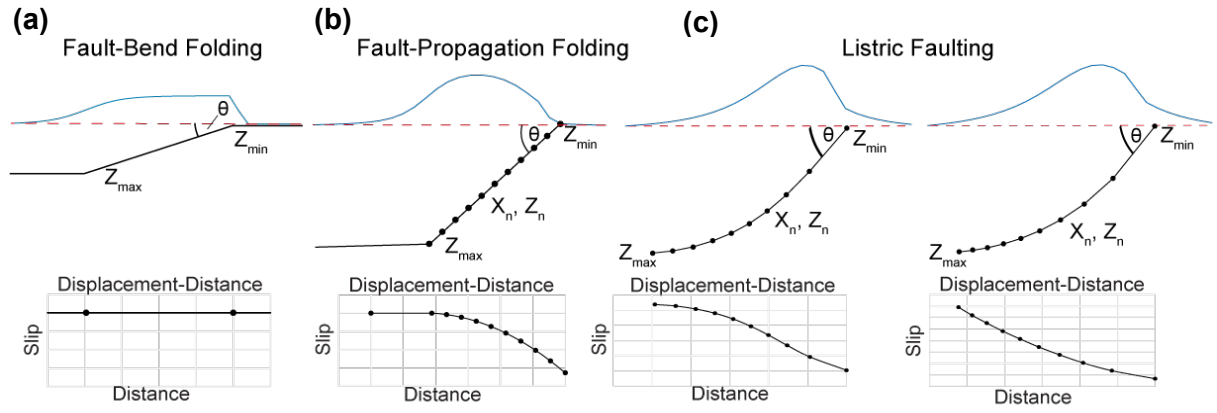

Figure 9. Model construction methods for (**a**) fault-bend fold, (**b**) fault-propagation fold, and (**c**) listric fault geometries showing the idealized surface displacement (blue) and with corresponding fault plane geometry (black). Displacement-distance plots are included for each. Models are not drawn to scale.

rooting to a horizontal detachment plane. An equivalent seismic moment across each segment was assumed to simulate incremental strain as a single event due to model limitations. The dip angle at the fault tip was user-defined, with each section decreasing linearly to zero at the base of the listric plane (**Fig 9c**). Two modes of slip distribution were employed to represent realistic fault configurations more accurately. That is, both idealized thrust faulting with orthogonal stress vectors, represented by a linear displacement gradient, and faulting with a non-negligible out-of-plane shear component, as suggested by the structural analysis (Section **3.2**), represented by a quadradic displacement gradient (Wickham, 1995; Hughes & Shaw, 2014), were modeled. The position of each segment (X_n, Z_n) was then calculated via multiple linear regression for a constant seismic moment with the user-defined parameters as determined by the following equation:

$$M_0 = D_n A \mu, \text{ where } A = \frac{x_n}{sin\theta_n}, \text{ and } \mu = const, \qquad [4]$$

$$\text{therefore, } M_0 = \frac{D_n\, x_n}{sin\theta_n} = const, \text{ with } Z_n = \frac{x_n}{tan\theta_n} \qquad [5]$$

A total of 26,044 listric fault configurations were iterated within the forward modelling.

5.1. Elastic Dislocation Model Results

Elastic dislocation solutions (Okada, 1992) to these inputs yielded a stress state and resulting surface deformation of the model grid in two dimensions (along the X–Z axes). Model solutions were iteratively refined to produce best-fit solutions defined by the RMSE between modeled surface deformation and the cross-sectional profiles taken earlier. The model domain was limited to the ridge belts' width to capture the topographic variations from the short-wavelength deformation (i.e., faulting and folding), without incorporating any lithospheric flexure signatures present. The goodness of fit was determined using minimization of an RMSE cost function as the modeled profile was shifted along the X- and Z-axes to achieve the best possible match with the observed profile. By shifting profiles along either axis, aspect ratios or geometry of the surface deformation were not altered. Model solutions with an RMSE value below 0.2, normalized by the range over the Z-axis, were regarded as acceptable fits.

Model results for six profiles across four ridge belts met the criterion for having an acceptable model fit to observed topography (**Fig. 10, Appendix C1-6**). Best-fit solutions for each profile were matched to the surface displacement from a listric fault plane rooting to a detachment zone, with depths ranging from 15.3 to 23.4 km (**Fig. 11**) with no apparent dependence on geographic location or elevation of the ridge belt. The values reported here represent the bootstrap mean value (n = 5000) (**Appendix C1-6**) with error bars giving the standard deviation for all model solutions below the accepted RMSE threshold within each ridge belt. These results show that a listric fault geometry best captures the observed surface deformation across all tested ridge belts.

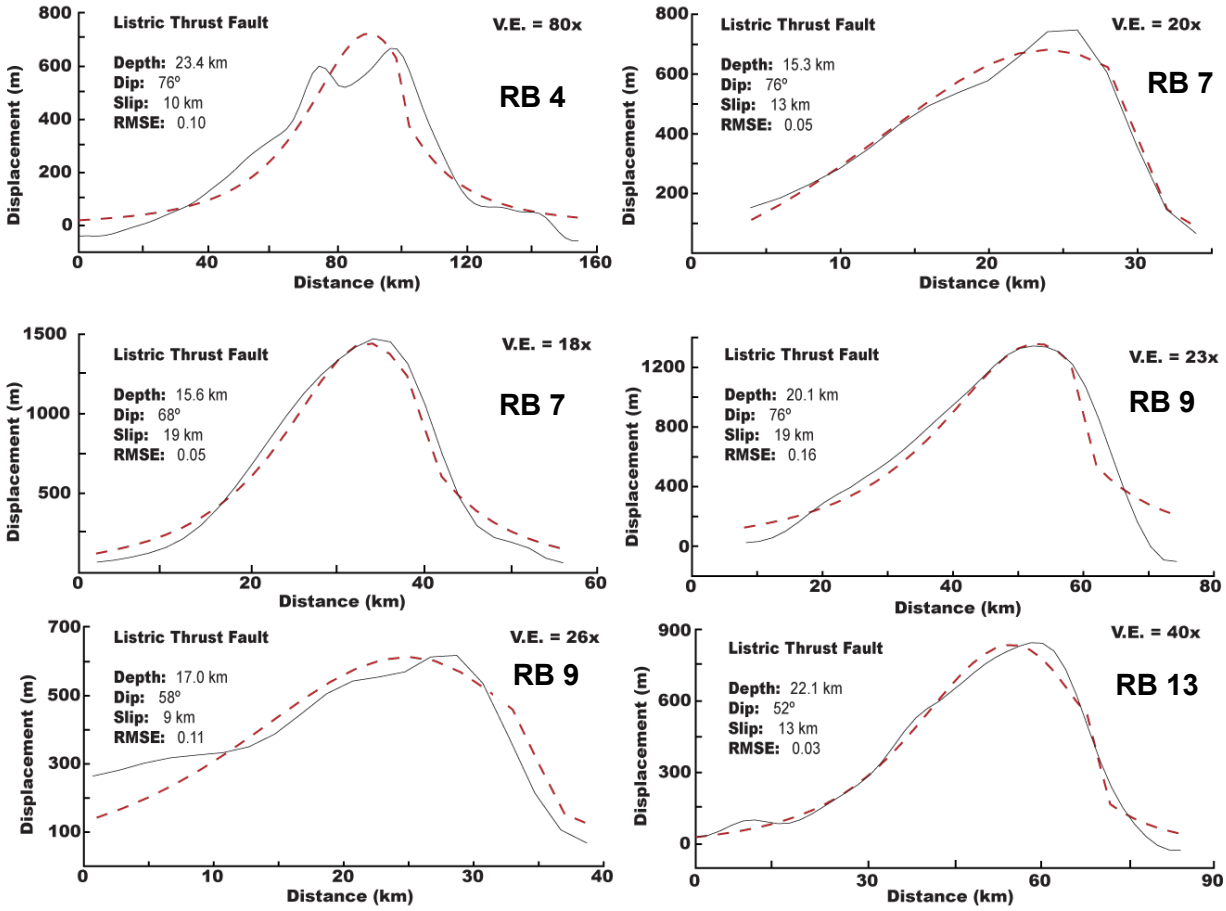

Figure 10. Elastic dislocation model results for profile best-fit solutions. Black profiles are observed topography; the red dotted lines represent the best-fit model solution. All results involve listric fault plane geometry with a quadratic slip displacement and a BDT depth of 15.3–23.4 km.

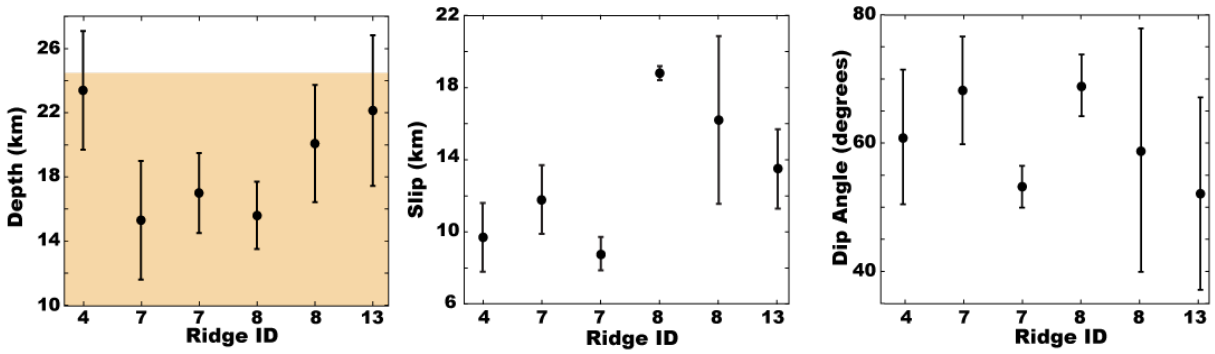

Figure 11. Best-fit model values for the dip, slip, and depth of each successful Coulomb model. Error bars give the standard deviation for across all input files for which there were acceptable results. Duplicate ridge ID numbers indicate different profiles along the same landform. The orange shaded region within the depth plot indicates the range of flexure model results.

6. Discussion

It is important to note the common occurrence of wrinkle ridges within the low-lying plains regions accompanying the ridge belts. Wrinkle ridges are ubiquitous throughout terrestrial bodies of the Solar System and denote distributed but low amounts of shortening strain (McGill, 1993; Campbell et al, 1994; Klimczak et al., 2019). In contrast to wrinkle ridges, however, ridge belts are much more spatially concentrated areas of deformation, and probably accommodate a substantially greater amount of shortening strain within concentrated bands of deformation (Solomon et al., 1992; Suppe & Connors, 1992; Young and Hansen, 2005). Thus, notable differences in scale and morphology set ridge belts apart from wrinkle ridges observed elsewhere on Venus and other terrestrial bodies, with these belts more comparable to orogenic belts seen on Earth (Campbell et al., 1983; Crumpler et al., 1986). We, therefore, regard ridge belts as complex systems of thrust fault duplexes within a relatively mechanically thin lithosphere, in contrast to shortening structures on other worlds that are often morphologically more simple, such as the

fault-propagation-fold “lobate scarps” on Mercury and Mars (e.g., Byrne et al., 2018).

6.1. Implications of Ridge Belt Structure

Compared with fold-and-thrust belts on Earth, the cross-sectional width of faulting observed in ridge belts is associated with a relatively low amount of vertical deformation. Aspect ratios (relief to width) throughout the ridge belts included in this study have a mean of 0.013%, comparable, but notably lower than those of fold-and-thrust belts on Earth (~0.04%). Exceptionally low aspect ratios such as these are taken to indicate a mechanically thin lithosphere, as high-standing topography cannot readily be mechanically supported. A thin mechanical lithosphere is also suggested by the topographic profiles we collected, in the form of flexural troughs denoting flexure of the elastic lithospheric in response to vertical loading. Given the low relief of the ridge belts examined (i.e., 330–830 m), their weight does not apply vertical stress upon the crust of the same magnitude as larger seamounts or mountain chains in the ocean basins on Earth. Nevertheless, flexural signatures are still observed, providing a first-order indication that the lithosphere is relatively mechanically thin.

The morphological resemblance between the cross-sectional shape of ridge belts to fault-displacement-gradient folding indicates that the belts were predominantly formed by orthogonal shortening. Primarily orthogonal shortening is supported by the abundance of thrust fault populations, striking within 10° of the host landform, relative to normal or strike-slip fault populations. Our interpretation of the observed pattern of thrust faulting is that the structural cores of ridge belts predominately consist of imbricated thrusts with overlying anticlinal folds. Anticlinal folds are observed in both the topographic data, a series of short-wavelength positive-relief superimposed upon the overall ridge belt profile, and the recognition of antithetic thrust pairs during mapping. Gently dipping imbricated thrust systems are a major element of fold-and-

thrust belts on Earth that root to shallow detachment planes (Problet & Lisle 2011).

Generally, consistent thrust fault orientations throughout individual ridge belts indicate that the stress field orientation has not changed greatly throughout belt formation. Although the strikes of thrust faults within a given ridge belt are relatively uniform, more variation is observed in folding wavelength, which is interpreted as an indication of heterogeneities within the mechanical properties of faults underlying the anticlines.

Observations of conjugate faulting, splay faults, and restraining bends within the examined ridge belts indicate some minor component of oblique compression (i.e., transpression), interpreted to reflect partitioning of transpressional strain, or shortening stress applied obliquely to preexisting fault planes. Dewey et al. (1998) noted that kinematic boundary conditions heavily influence zones of oblique compression. The elevated surface temperatures (~460 C) and correspondingly low depth to the BDT zone predicted by our numerical models suggest that the base of the mechanical lithosphere could represent a kinematic boundary influencing ridge belt structure. We note, however, that the lithology of lowland plains areas is basaltic, probably composed of successive volcanic deposits as shown by radar observation (eg., Barsukov et al., 1986, Frank and Head, 1990; Campbell & Rogers, 1994). It is possible that layering within volcanic units can form sufficient stratigraphic differences at depth to impart a mechanical boundary.

6.2. Mechanical Thickness of the Lithosphere

The analytical solutions to lithospheric flexural response and the elastic dislocation modeling of ridge belt formation are consistent with the hypothesis that ridge belts have formed within a relatively thin lithosphere. The determinations of lithospheric thickness from both modeling approaches generally agree with previous modeling and theoretical surveys that

predicted a relatively thin mechanical lithosphere as a function of high surface temperatures at Venus (Suppe & Connors, 1992; Buck, 1992; James et al., 2013; Ghail 2015).

Elastic dislocation models predict a lithospheric thickness of 15.3–23.4 km with faults possessing a listric geometry. Such geometry is commonly related to shortening systems that root to a shallow detachment plane (e.g., Buchanan & McClay, 1991; Peterson et al., 2020). Given that the flexure results indicate a mechanical thickness up to 14.5 km, this detachment may represent the BDT zone, and thus the thickness of the mechanical lithosphere. Assuming a comparable increase in confining pressure with depth to Earth, the depth to BDT can be taken to reflect a thermal boundary layer from which the corresponding isotherm can be deduced. We thus leverage our findings of the lithosphere' mechanical structure returned by our assessments of ridge belts to examine the present thermal structure of the low-lying plains regions.

The maximum temperature possible at the base of the lithosphere is dependent on rock type. With the few constraints available for the composition of the Venus crust, we elected to use the temperature at the base of mature oceanic lithosphere on Earth, 1350 ± 275° C (Parsons & Sclater, 1977; Solomon & Head, 1982), below which we can assume deformation must be dominated by plastic processes for all possible lithologies. A first-order approximation of thermal gradients was calculated, giving a range of 30.8 to 63.8°C km^{-1}, with a mean of 42.9°C km^{-1}. These values are comparable with regions near spreading centers on Earth corresponding to an oceanic lithospheric thickness of ~32 km. Thermal gradients reported here exceed previous global estimates (Solomon & Head, 1982; James et al., 2013). The values for the depth to the BDT zone identified with elastic dislocation modeling are minima, these values represent an upper bound for calculated thermal gradients.

Given the temperature at the Venus surface, the basaltic lithosphere's thickness could

reasonably be compared to that of younger oceanic crust. For the suite of modeled mechanical lithospheric thickness values estimated in this study, the equivalent age of oceanic lithosphere corresponding to said thickness was determined with a simple half-space cooling model. The half-space cooling model, which relates the thickness of oceanic lithosphere to approximate age, was used because of the built-in assumptions that the lithosphere is asthenospheric material cooled conductively and that the rate of cooling is independent of thermal boundary conditions, which are relatively poorly constrained on Venus.

Thickness estimated from flexure solutions (5.7–14.5 km) is comparable to the thinnest portions of the young oceanic lithosphere, where "young" here is less than 2 Mya. Equivalent age estimates with elastic dislocation models (15.3–23.4 km) place the oceanic lithosphere's age at less than 10 Ma. Approximate ages largely agree with calculations of thermal gradients equivalent to oceanic lithosphere near spreading centers. Therefore, ridge belts likely reside in basaltic plains that, in addition to being subject to high surface temperature, may also have mechanical thickness influenced by a relatively high heat flux across the crust-mantle boundary in much the same way as young oceanic lithosphere on Earth.

Although the mean surface temperature (~460°C) at Venus is well known and is thus a well-established upper boundary condition, our lithospheric thickness estimates (that essentially represent the depth to the 1300° C isotherm) were used to determine the lower thermal boundary condition, or basal heat flow. Under the assumption that the interior of Venus is compositionally similar to that of Earth, estimates for the global heat flux can be calculated by scaling the global heat flux of Earth to Venus (Pollack et al., 1993; Turcotte et al., 1999). This first-order approximation places the global heat flux of Venus around 36 TW or a heat flux of 76 mW m^{-2}. Venus, however, is considered to be within a stagnant lid regime (e.g., Solomatov & Moersei,

1996) wherein the lithosphere is coupled to a high-viscosity mantle that convects at a slow enough rate for heat transport to be predominately via conductive cooling, in contrast with the convective heat transport afforded by plate tectonics on Earth (Anderson, 1981; Solomon & Head, 1982; Ghail, 2015). A purely stagnant lid regime, in which the sole mechanism of heat transfer is conduction, can remove anywhere from 8 to 20 mW m^{-2} (Solomatov & Moresi, 1996; Reese et al., 1998). We thus constructed simple geotherms under the range of different basal heat flow values reported in previous studies to calculate a heat flux consistent with the lithospheric thickness values we found.

Assuming a constant heat flow and little to no erosion or deposition of a hypothetical column of rock (i.e., a static upper boundary condition), an equilibrium geotherm can be calculated along a one-dimensional profile as determined by the radiogenic heat generation, A, and thermal conductivity, k, of the crustal material:

$$\frac{\partial^2 T}{\partial z} = -\frac{A}{k} \qquad [6]$$

Geochemical data from the Soviet Venera 8, 9, and 10 landing sites showed abundances of U, Th, and K (Surkov, 1977, Surkov et al., 1977), whereas samples from the Venera 13 and 14 sites indicated high amounts of K_2O (Barsukov, 1982). Mineralogical profiles reported in these studies are thus comparable to tholeiites and alkali basalts, respectively (Solomon & Head, 1982). Radiogenic heat generation, A, for either rock type was thus used in the calculation of geotherms. Equation 6 can be solved under boundary conditions where i) temperature $T = 460$ at $z = 0$ and ii) heat flow $Q = -Q_d$ at $z = d$, representing heat flowing from the mantle into the base of the crust. Equation 6 can then be integrated twice to give:

$$T = -\frac{A}{2k}z^2 + \frac{Q_d + Ad}{k}z + 460 \qquad [7]$$

Geotherms were calculated under a range of basal heat flows used by earlier theoretical studies

for columns within these two lithologies, reflecting differences in radiogenic heat production (**Fig 12**). Solutions in which the geotherms intersect the range of lithospheric thickness estimates and the 1350 ± 275° C isotherm were taken to reflect a basal heat flow that agrees with the mechanical structure inferred earlier in this study.

When examining geotherms calculated from lithospheric flexure solutions (**Fig 12**), a higher basal heat flow value is estimated from elastic dislocation analysis. Results with a heat flow closer to 76 mW m^{-2} matched with observed crustal thickness values, closer to the first-order approximations of mantle heat flow on the comparative basis with Earth. Calculated heat transfer across the crust–mantle boundary is much higher than simple stagnant-lid conductive models predict, however, and suggest that more heat is emanating from the interior in the lowlands where the ridge belts are situated than is currently recognized. Thus, these results suggest that some other mechanism of heat transfer beyond simple conduction within a stagnant lid regime may account for a basal heat flow greater than 20 mW m^{-2}, the cause of which is beyond the scope of this study.

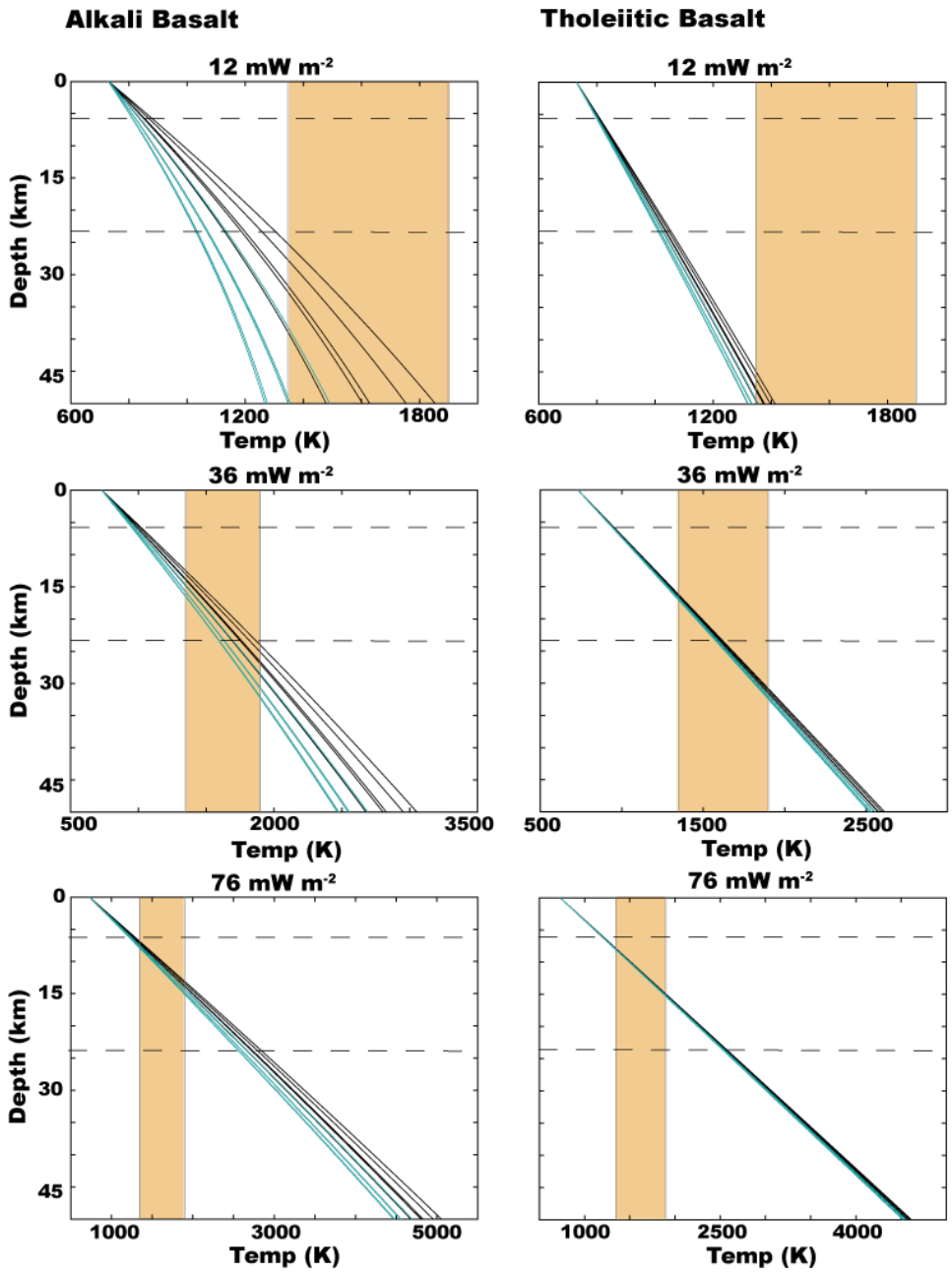

Figure 12. Geotherms for both alkali and tholetiic basalt columns under different basal heat flow values. Each profile represents a crust of thickness, *d*, as determined by the flexure solutions (blue) and elastic dislocation models (black). The orange region represents the expected temperature at the base of the lithosphere (1573° ± 275 K) and horizontal dashed lines represent estimated lithospheric thickness depths from flexural and elastic dislocation modeling analyses.

6.3. Model Limitations

As pointed out by Hughes and Shaw (2014), naturally occurring tectonic structures are sufficiently complex or have experienced multiple deformation sequences in their history such that a single model solution cannot perfectly replicate them. Thus, for example, the slip values indicated by our model results likely under-represent the shortening strain accommodated by ridge belts since these structures appear to comprise many imbricated component thrust faults.

Results show a listric geometry best explains the surface deformation observed for all ridge belts modeled in this study. To best explain the topography of ridge belts, modeled listric fault geometries required a large accumulation of slip at the base of the fault plane, resulting in greater fault penetration depths, than thickness estimates within the lithospheric flexure portion of this study. This discrepancy is likely a result of modeled fault planes being constructed as a single slip event, with models featuring individual segments of equivalent seismic moment and tapered slip. To conserve seismic moment with a lesser slip amount, shallower segments with greater dip angles are longer, corresponding to a greater vertical reach and forcing the segments with higher slip amounts to greater depths. Additionally, the use of an elastic deformation model within an infinite isotropic half-space minimizes unrealistic edge-effect model behavior.

However, this model setup also has the adverse effect of not incorporating thermally dependent changes in viscoelastic properties throughout the crust instead of simulating solely elastic behavior. Within a real-world setting, the increase in temperature and pressure with depth has a major effect on rock deformation behavior. Numerical model solutions are, however, a single element within this study. Although that portion of this work faces the limitations of any modeling approach, we find that our numerical results agree with those found via morphological and structural analyses, which together provide strong evidence that ridge belts are situated

within a mechanically thin lithosphere.

There is a noticeable difference (~9 km) between the predicted depth value for the BDT between the lithospheric flexure and elastic dislocation model results. A probable cause for this disparity is the crustal thickening involved in forming the ridge belts. We observe the regional isostatic response in our flexure models predicated upon a substantial amount of crustal thickening. As we model the fault geometry from surface displacement, we are doing so within the thickened portion of the crust, and therefore are looking at the local maxima of lithospheric thickness compared to the thickness of the lithosphere in the surrounding plains. With our interpretation of ridge belts on Venus as analogs to fold-and thrust-belts on Earth, an approximation for the difference in thickness under ridge belts versus the surrounding plains was estimated by determining the hypothetical depth of the crustal root. Assuming Airy isostasy and using the same density values employed for the flexure portion of this study, we estimate a root depth of ~4km, explaining almost half of the observed disparity.

7. Conclusion

We find that the morphology, structure, and surface deformation exhibited by our study ridge belts on Venus are all consistent with these features to have formed within regions of mechanically thin lithosphere within the Venus lowlands. We interpret ridge belts as complex systems of imbricate thrust fault duplexes and conjugate faulting akin to fold-and-thrust belts on Earth. Subsequent modeling of the brittle-ductile transition depth by curve fitting of the lithospheric response to crustal loading, and surface deformation in an elastic medium returns estimates for the mechanical lithospheric thickness of fewer than 24 kilometers (in comparison to depths on Earth of 25–40 km). Our results agree with earlier predictions of mechanical thickness calculated from yield strength envelopes by Buck (1992) and Ghail (2015).

Plate tectonics on Earth is characterized by major deformation concentrated within relatively narrow bands at plate margins. Although plate tectonics do not appear to operate today on Venus, concentrated shortening deformation localized within a narrow zone along major fault planes is notably different from the more common regional-scale crustal shortening observed on other terrestrial bodies elsewhere in the solar system in the form of wrinkle ridges. Future missions to Venus should acquire yet higher resolution radar image and topographic data than those currently available to verify the results we report here and to enable additional ridge belts to be studied in this manner.

REFERENCES

Anderson, D. L. (1981). Plate tectonics on Venus. *Geophysical Research Letters*, *8*(4), 309-311.

Anderson, F. S., & Smrekar, S. E. (2006). Global mapping of crustal and lithospheric thickness on Venus. *Journal of Geophysical Research E: Planets*, *111*(8), 1–20. https://doi.org/10.1029/2004JE002395

Anderson, F. S., & Smrekar, S. E. (2006). Global mapping of crustal and lithospheric thickness on Venus. *Journal of Geophysical Research E: Planets*, *111*(8), 1–20. https://doi.org/10.1029/2004JE002395

Balcerski, J. A., & Byrne, P. K. (2018, November). Fault Analysis of Venus Ridge Belts Using Stereo-Derived Topography. In *16th Meeting of the Venus Exploration and Analysis Group (VEXAG)* (Vol. 16, No. 2137, p. 8012).

Balcerski, J. A., & Byrne, P. K. (2018, March). High-Resolution Ridge Belt Morphology at Dylacha Dorsa. In *Lunar and Planetary Science Conference* (No. 2083, p. 2735).

Barsukov, V. L., Basilevsky, A. T., Burba, G. A., Bobinna, N. N., Kryuchkov, V. P., Kuzmin, R. O., ... & Akim, E. L. (1986). The geology and geomorphology of the Venus surface as revealed by the radar images obtained by Veneras 15 and 16. *Journal of Geophysical Research: Solid Earth*, *91*(B4), 378-398.

Barsukov, V. L., Surkov, I. A., Moskaleva, L. P., Shcheglov, O. P., Khariukova, V. P., Manvelian, O. S., & Perminov, V. G. (1982). Geochemical studies of the surface of Venus by the Venera 13 and Venera 14 probes. *Geokhimiia*, 899-919.

Basilevsky, A. T., & Head, J. W. (2003). The surface of Venus. *Reports on Progress in Physics*, *66*(10), 1699.

Bilotti, F., & Suppe, J. (2014). *Global distribution of wrinkle ridges on Venus ; relationship to long- wavelength topography and gravity The Global Distribution of Wrinkle Ridges on Venus*. *January 1993*.

Buchanan, P. G., & McClay, K. R. (1991). Sandbox experiments of inverted listric and planar fault systems. *Tectonophysics*, *188*(1-2), 97-115.

Buck, W. R. (1992). Global decoupling of crust and mantle: implications for topography, geoid and mantle viscosity on Venus. *Geophysical research letters*, *19*(21), 2111-2114.

Byrne, P. K., Klimczak, C., McGovern, P. J., Mazarico, E., James, P. B., Neumann, G. A., Zuber, M. T., & Solomon, S. C. (2015). Deep-seated thrust faults bound the Mare Crisium

lunar mascon. *Earth and Planetary Science Letters*, *427*, 183–190. https://doi.org/10.1016/j.epsl.2015.06.022

Byrne, Paul K. "The Tectonic Character of Mercury." *Mercury: the view after Messenger*, by Christian Klimczak and A. M. Celâl Sengör, vol. 21, Cambridge University Press, 2018, pp. 249–286.

Campbell, B. A., & Rogers, P. G. (1994). Bell Regio, Venus: integration of remote sensing data and terrestrial analogs for geologic analysis. *Journal of Geophysical Research*, *99*(E10), 153–171. https://doi.org/10.1029/94je01862

Campbell, Bruce A. (1994). Merging Magellan Emissivity and SAR Data for Analysis of Venus Surface Dielectric Properties. *Icarus*, *112*(1), 187–203. https://doi.org/10.1006/icar.1994.1177

Chapple, W. M. (1978). Mechanics of thin-skinned fold-and-thrust belts. *Geological Society of America Bulletin*, *89*(8), 1189-1198.

Corredor, F., Shaw, J. H., & Bilotti, F. (2005). Structural styles in the deep-water fold and thrust belts of the Niger Delta. *AAPG bulletin*, *89*(6), 753-780.

Davis, G. H., Reynolds, S. J., & Kluth C. (2012). Thrust Fault Systems. In *Structural geology of rocks and regions* (3rd ed., pp. 305-320). Hoboken, NJ: John Wiley & Sons.

Dewey, J. F., Holdsworth, R.E., & Strachan, R. A. (1998). Transpression and transension zones. *Geological Society , London, Special Publications, 135*(1), 1-14. Doi: 10.1144/gsl.sp.1998.135.01.01

Ford, J. P. (1993). *Guide to Magellan image interpretation.* National Aeronautics and Space Administration, Jet Propulsion Laboratory, California Institute of Technology.

Ford, P. G. (1994). Radar scattering properties of steep-sided domes on Venus. *Icarus, 112*(1), 204-218. doi:10.1006/icar.1994.1178

Fowler, C. R. (2012). *The solid Earth: An introduction to global geophysics* (2nd ed.). Cambridge, U.K.: Cambridge University Press.

Frank, S. L., & Head, J. W. (1990). Ridge belts on Venus: Morphology and origin. *Earth, Moon, and Planets, 50*(1), 421-470.

Ghail, R. (2015). Rheological and petrological implications for a stagnant lid regime on Venus. *Planetary and Space Science*, *113–114*, 2–9. https://doi.org/10.1016/j.pss.2015.02.005

Hansen, V. L. (2018). Global tectonic evolution of Venus, from exogenic to endogenic over

time, and implications for early Earth processes. *Philosophical Transactions of the Royal Society A: Mathematical, Physical and Engineering Sciences*, *376*(2132). https://doi.org/10.1098/rsta.2017.0412

Herrick, R. R., Stahlke, D. L., & Sharpton, V. L. (2012). Fine-scale Venusian topography from Magellan stereo data. *Eos*, *93*(12), 125–126. https://doi.org/10.1029/2012EO120002

Hughes, A. N., Benesh, N. P., & Shaw, J. H. (2014). Factors that control the development of fault-bend versus fault-propagation folds: Insights from mechanical models based on the discrete element method (DEM). *Journal of Structural Geology*, *68*(PA), 121–141. https://doi.org/10.1016/j.jsg.2014.09.009

Hughes, A. N., & Shaw, J. H. (2014). Fault displacement-distance relationships as indicators of contractional fault-related folding style. *AAPG Bulletin*, *98*(2), 227–251. https://doi.org/10.1306/05311312006

Ivanov, M. A., & Head, J. W. (2011). Global geological map of Venus. *Planetary and Space Science*, *59*(13), 1559–1600. https://doi.org/10.1016/j.pss.2011.07.008

Ivanov, M. A., & Head, J. W. (2013). The history of volcanism on Venus. *Planetary and Space Science*, *84*, 66–92. https://doi.org/10.1016/j.pss.2013.04.018

James, P. B., Zuber, M. T., & Phillips, R. J. (2013). Crustal thickness and support of topography on Venus. *Journal of Geophysical Research E: Planets*, *118*(4), 859–875. https://doi.org/10.1029/2012JE004237

Klimczak, C., Byrne, P. K., Celâl Şengör, A. M., & Solomon, S. C. (2019). Principles of structural geology on rocky planets. *Canadian Journal of Earth Sciences*, *56*(12), 1437–1457. https://doi.org/10.1139/cjes-2019-0065

Klimczak, C., Kling, C. L., & Byrne, P. K. (2018). Topographic Expressions of Large Thrust Faults on Mars. *Journal of Geophysical Research: Planets*, *123*(8), 1973–1995. https://doi.org/10.1029/2017JE005448

Kutil, R. (2012). Biased and unbiased estimation of the circular mean resultant length and its variance. *Statistics*, *46*(4), 549–561. https://doi.org/10.1080/02331888.2010.543463

McGill, G. E. (1993). Wrinkle ridges, stress domains, and kinematics of Venusian plains. *Geophysical Research Letters*, *20*(21), 2407-2410.

McGill, G. E., & Campbell, B. A. (2006). Radar properties as clues to relative ages of ridge belts and plains on Venus. *Journal of Geophysical Research E: Planets*, *111*(12), 1–11.

https://doi.org/10.1029/2006JE002705

Mitra, S. (1986). Duplex structures and imbricate thrust systems: geometry, structural position, and hydrocarbon potential. *AAPG bulletin*, *70*(9), 1087-1112.

O'Rourke, J. G., & Smrekar, S. E. (2018). Signatures of Lithospheric Flexure and Elevated Heat Flow in Stereo Topography at Coronae on Venus. *Journal of Geophysical Research: Planets*, *123*(2), 369–389. https://doi.org/10.1002/2017JE005358

Ojeda, G. Y., & Whitman, D. (2002). Effect of windowing on lithosphere elastic thickness estimates obtained via the coherence method: Results from northern South America. *Journal of Geophysical Research: Solid Earth*, *107*(B11), ETG 3-1-ETG 3-12. https://doi.org/10.1029/2000jb000114

Okada, Y. (1992). Internal deformation due to shear and tensile faults in a half-space. *Bulletin - Seismological Society of America*, *82*(2), 1018–1040.

Parsons, B., & Sclater, J. G. (1977). An analysis of the variation of ocean floor bathymetry and heat flow with age. *Journal of geophysical research*, *82*(5), 803-827.

Peterson, G. A., Johnson, C. L., Byrne, P. K., & Phillips, R. J. (2020). Fault Structure and Origin of Compressional Tectonic Features Within the Smooth Plains on Mercury. *Journal of Geophysical Research: Planets*, *125*(7), 1–18. https://doi.org/10.1029/2019JE006183

Phillips, R. J., Raubertas, R. F., Arvidson, R. E., Sarkar, I. C., Herrick, R. R., Izenberg, N., & Grimm, R. E. (1992). Impact craters and Venus resurfacing history. *Journal of Geophysical Research: Planets*, *97*(E10), 15923-15948.

Poblet, J., & Lisle, R. J. (2011). Kinematic evolution and structural styles of fold-and-thrust belts. *Geological Society Special Publication*, *349*, 1–24. https://doi.org/10.1144/SP349.1

Pollack, H. N., Hurter, S. J., & Johnson, J. R. (1993). Heat flow from the Earth's interior: Analysis of the global data set. *Reviews of Geophysics*, *31*(3), 267–280. https://doi.org/10.1029/93RG01249

Reese, C. C., Solomatov, V. S., & Moresi, L. N. (1998). Heat transport efficiency for stagnant lid convection with dislocation viscosity: Application to Mars and Venus. *Journal of Geophysical Research: Planets*, *103*(E6), 13643-13657.

Schultz, R. A. (1993). Brittle strength of basaltic rock masses with applications to Venus. *Journal of Geophysical Research*, *98*(E6). https://doi.org/10.1029/93je00691

Schultz, Richard A., Okubo, C. H., & Wilkins, S. J. (2006). Displacement-length scaling

relations for faults on the terrestrial planets. *Journal of Structural Geology*, *28*(12), 2182–2193. https://doi.org/10.1016/j.jsg.2006.03.034

Schultz, R. A., & Watters, T. R. (2001). Forward mechanical modeling of the Amenthes Rupes thrust fault on Mars. *Geophysical Research Letters*, *28*(24), 4659-4662.

Solomatov, V. S., & Moresi, L. N. (1996). Stagnant lid convection on Venus. *Journal of Geophysical Research: Planets*, *101*(E2), 4737-4753.

Solomon, S. C., Smrekar, S.E., Bindschadler, D.L., Grimm, R.E., Kuala, W.M., McGill, G. E., Phillips, R. J., Saunders, R.S., Schubert, G., Squyres, S.W., Stofan, E. R. (1992). Venus tectonics: an overview of Magellan observations. *Journal of Geophysical Research*, *97*(E8). https://doi.org/10.1029/92je01418

Solomon, Sean C., & Head, J. W. (1982). Mechanisms for lithospheric heat transport on Venus: Implications for tectonic style and volcanism. *Journal of Geophysical Research*, *87*(B11), 9236. https://doi.org/10.1029/jb087ib11p09236

Squyres, S. W., Jankowski, D. G., Simons, M., Solomon, S. C., Hager, B. H., & McGill, G. E. (1992). Plains tectonism on Venus: The deformation belts of Lavinia Planitia. *Journal of Geophysical Research: Planets*, *97*(E8), 13579-13599.

Surkov, I. A. (1977). Geochemical studies of Venus by Venera 9 and 10 automatic interplanetary stations. In *Lunar and Planetary Science Conference Proceedings* (Vol. 8, pp. 2665-2689).

Surkov, I. A., Kirnozov, F. F., Glazov, V. N., & Fedoseev, G. A. (1976, June). Investigations of venusian gamma-radiation by venera 9 and venera-10. In *COSPAR Meeting*.

Suppe, J. (1983). Geometry and kinematics of fault-bend folding. *American Journal of Science*, *283*(7), 684–721. https://doi.org/10.2475/ajs.283.7.684

Suppe, J., & Connors, C. (1992). Critical taper wedge mechanics of fold-and-thrust belts on Venus: initial results from Magellan. *Journal of Geophysical Research*, *97*(E8). https://doi.org/10.1029/92je01164

Turcotte, D. L., Morein, G., Roberts, D., & Malamud, B. D. (1999). Catastrophic Resurfacing and Episodic Subduction on Venus. *Icarus*, *139*(1), 49–54. https://doi.org/10.1006/icar.1999.6084

Wickham, J. (1995). Fault displacement-gradient folds and the structure at Lost Hills, California (USA). *Journal of Structural Geology*, *17*(9), 1293-1302.

Williams, C. A., Connors, C., Dahlen, F. A., Price, E. J., & Suppe, J. (1994). Effect of the brittle-

ductile transition on the topography of compressive mountain belts on Earth and Venus. *Journal of Geophysical Research*, *99*(B10). https://doi.org/10.1029/94jb01407

Young, D. A., & Hansen, V. L. (2005). Poludnista Dorsa, Venus: History and context of a deformation belt. *Journal of Geophysical Research E: Planets*, *110*(3), 1–16. https://doi.org/10.1029/2004JE002280

Zuber, M. T., & Parmentier, E. M. (1990). On the relationship between isostatic elevation and the wavelengths of tectonic surface features on Venus. *Icarus*, *85*(2), 290–308. https://doi.org/10.1016/0019-1035(90)90118-S

APPENDICES

Appendix A

Additional Topographic Profiles

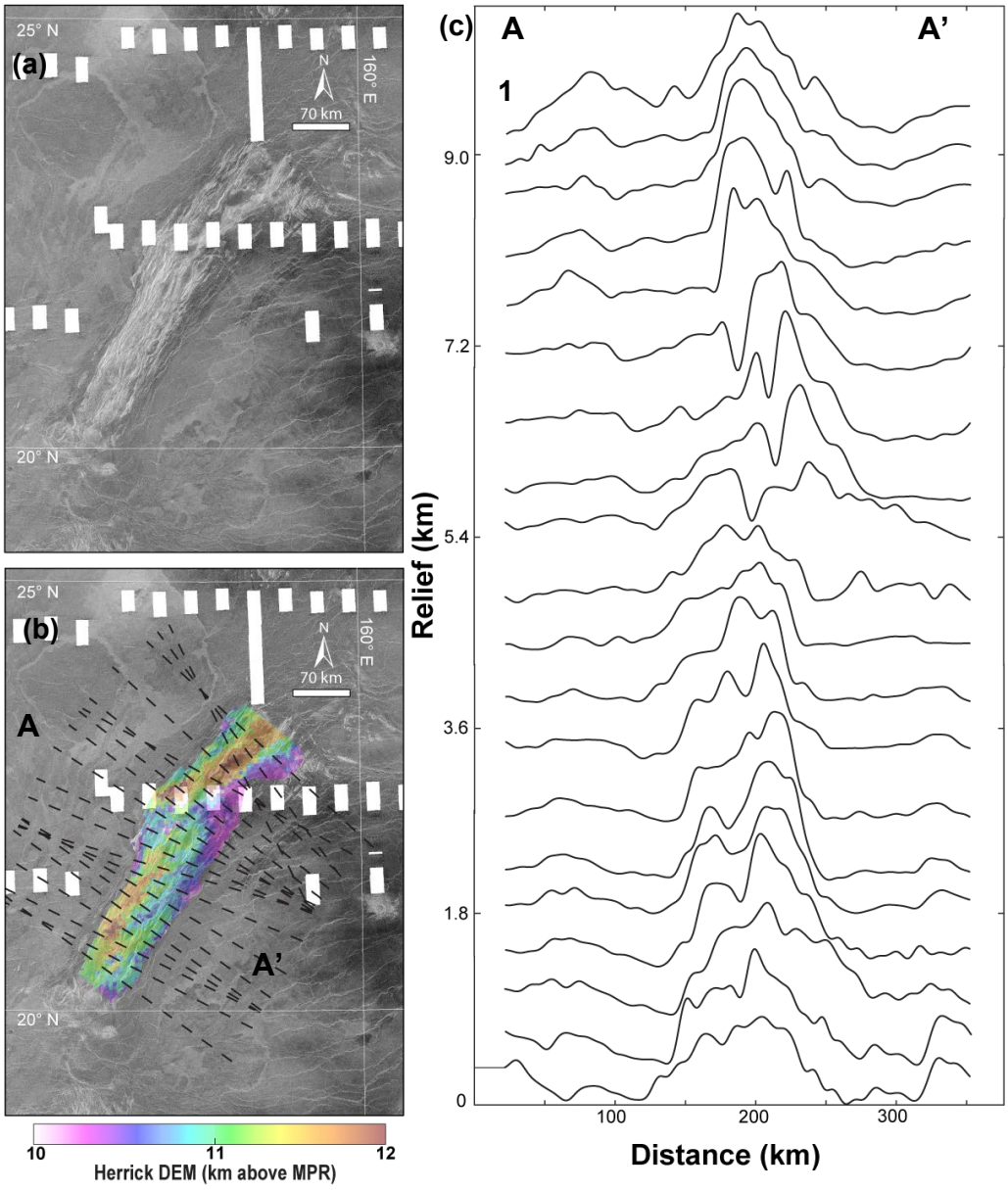

Figure A1. Example of a ridge belt (**a**) within the Herrick DEM (**b**). Topographic coverage is provided exclusively for the area of the ridge belts itself, for which a weighted hypsometric curve was calculated for relief. Corresponding topographic profiles are shown by the dashed black lines, with A and A' denoting the orientation (**c**). Profiles progress from top to bottom (c) as Northeast to Southwest on the map (**b**)

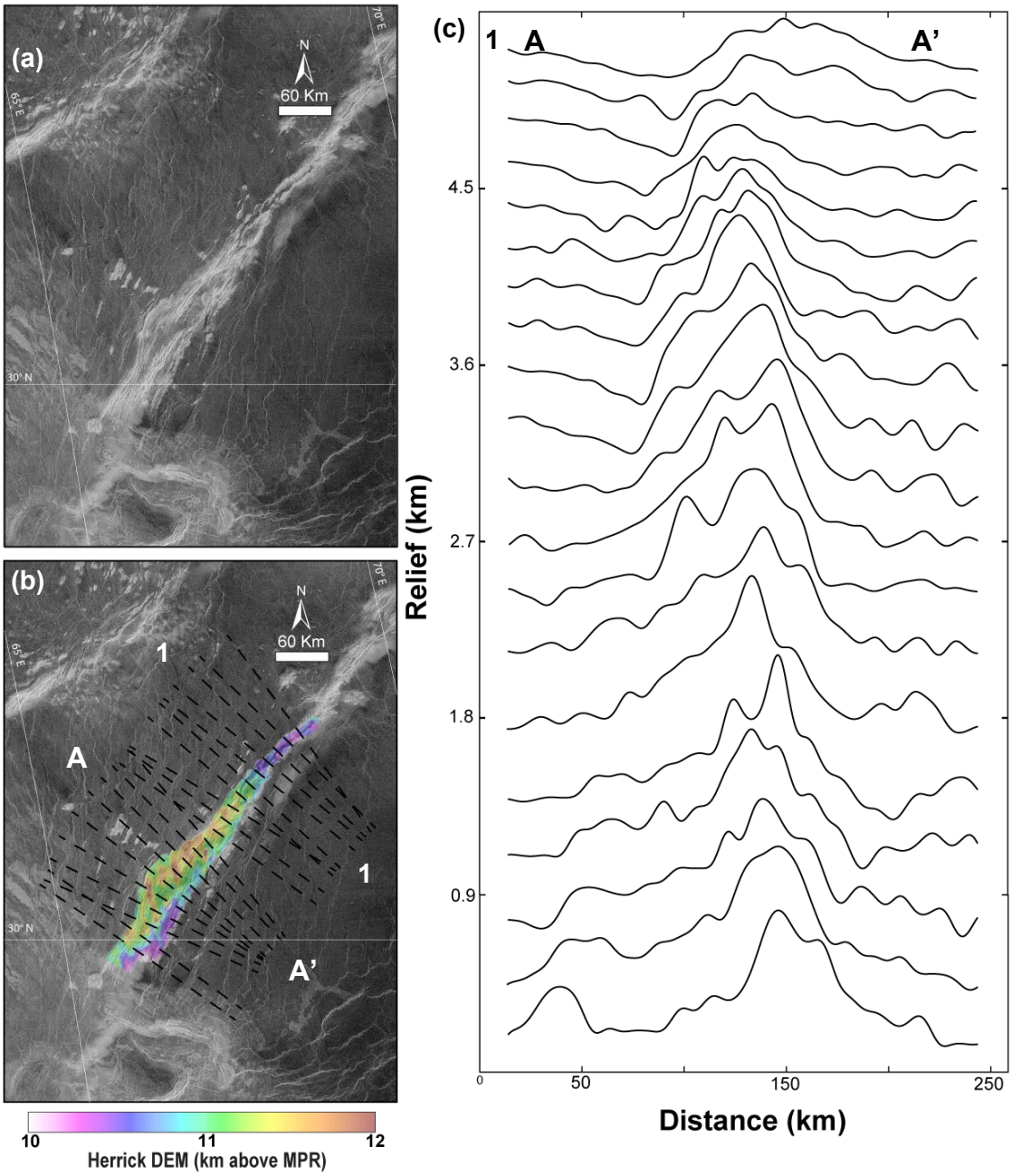

Figure A2. Example of a ridge belt (**a**) within the Herrick DEM (**b**). Topographic coverage is provided exclusively for the area of the ridge belts itself, for which a weighted hypsometric curve was calculated for relief. Corresponding topographic profiles are shown by the dashed black lines, with A and A' denoting the orientation (**c**). Profiles progress from top to bottom (c) as Northeast to Southwest on the map (**b**)

Appendix B

Additional Structural Maps of Ridge Belts

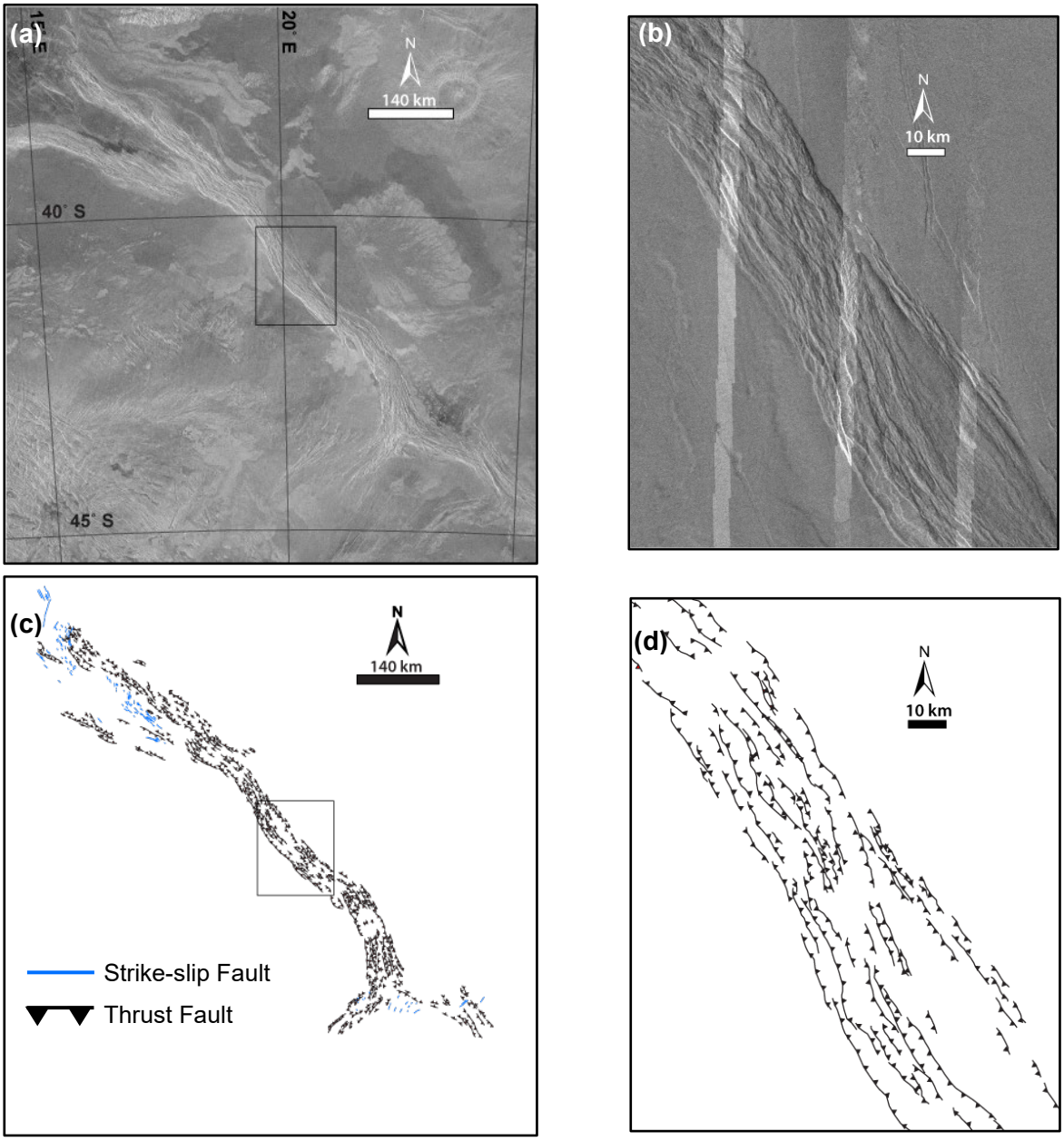

Figure B1. (**a**) A ridge belt (RB 10) centered about 41° S 21° E as seen within the left-look SAR survey. Black inset box gives the location of (**b**), a closer perspective of the tectonic fabric of which RB 10 consists (**c**). Blue faults represent strike-slip faulting along the lateral edges of the landform while black traces represent thrust faulting. Structural interpretation of RB 10 showing the prevalence of thrust faulting with the corresponding closer perspective (**d**). Black fault traces represent thrust faults with the teeth giving the inferred dip direction

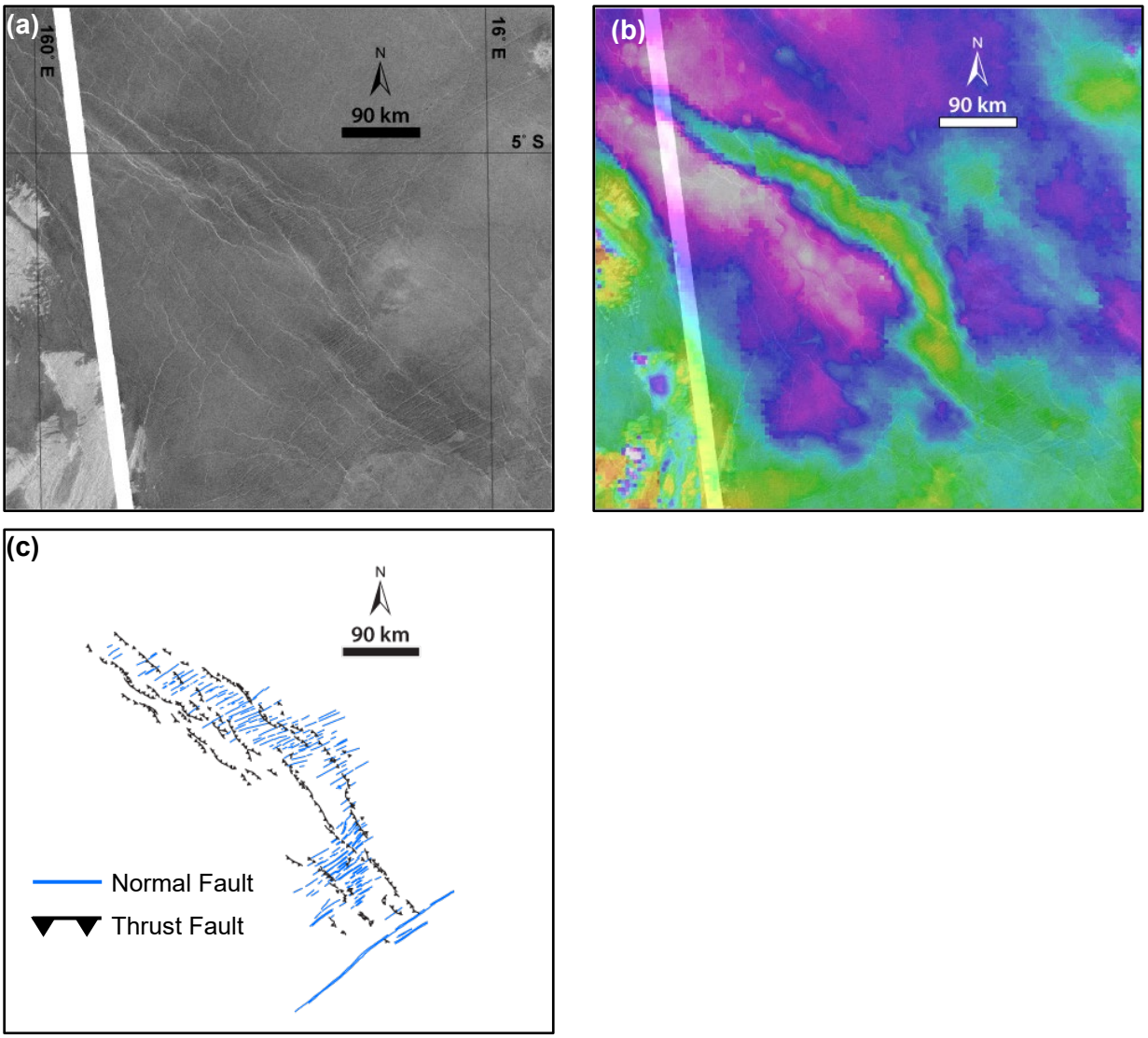

Figure B2. (**a**) A ridge belt (RB 13) centered about 5° S 162° E as seen within the left-look SAR survey. (**b**) RB 13 as it appears within the higher-resolution DEM displaying the characteristic elevated topography. (**c**) Structural mapping of RB 13 shows normal faults in blue and thrust faulting in black. Findings suggest a much greater amount normal faulting, offset in an echelon manner, than other ridge belts within this study.

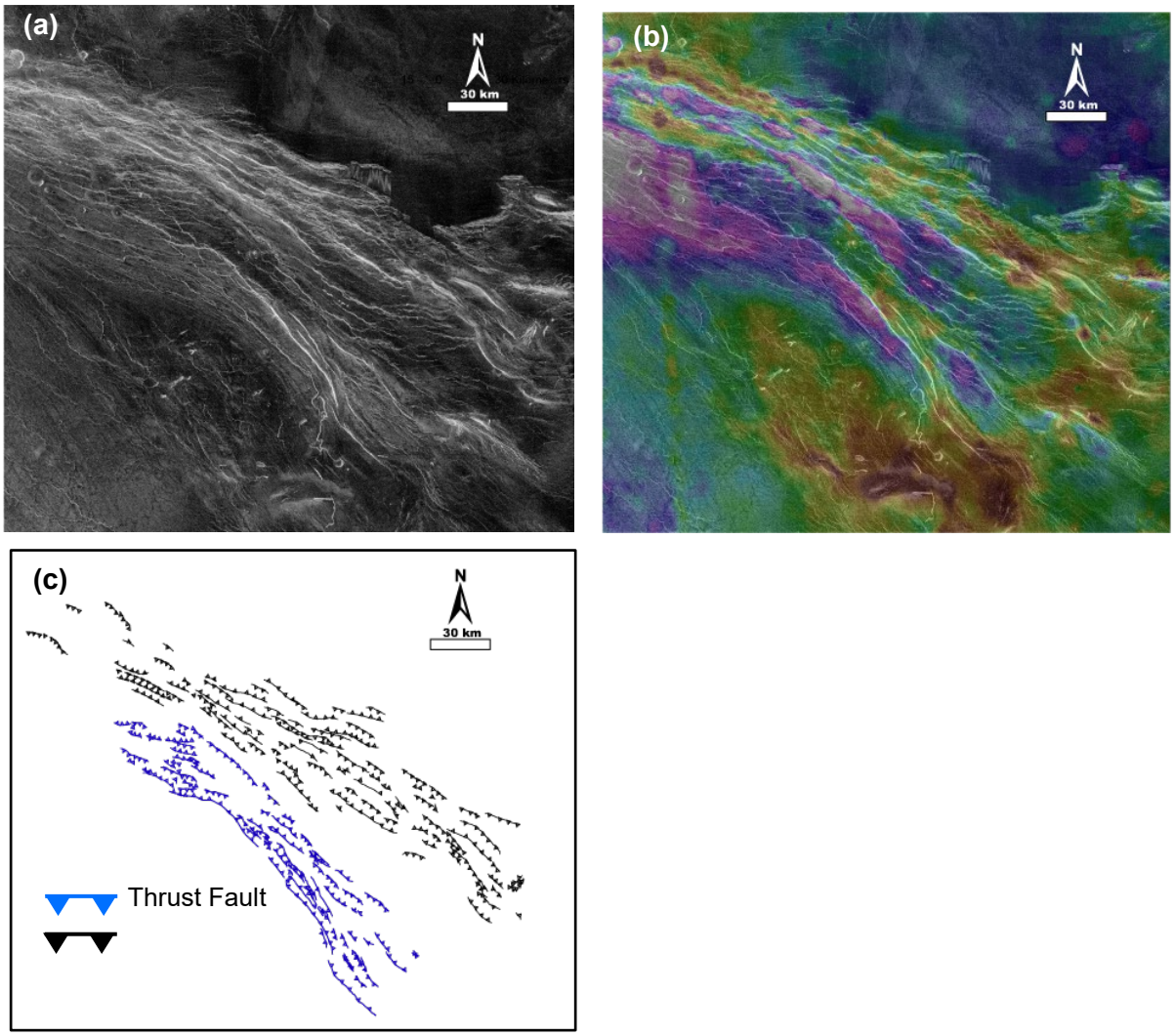

Figure B3. Two ridge belts in close proximity (RB 6 and 7) seen within the left-look Magellan SAR data (**a**) and corresponding higher-resolution DEM coverage displaying characteristic elevated topography (**b**). A structural interpretation of the faulting observed in both ridge belts (**c**). Findings suggest that unlike other ridge belts in this study, these ridge belts are solely thrust fault related landforms, with no clear evidence of transpressional strain. Thrust faulting within these landforms, while similarly oriented, show a high degree of variability with spacing.

Appendix C

Supporting Material for Elastic Dislocation Modeling

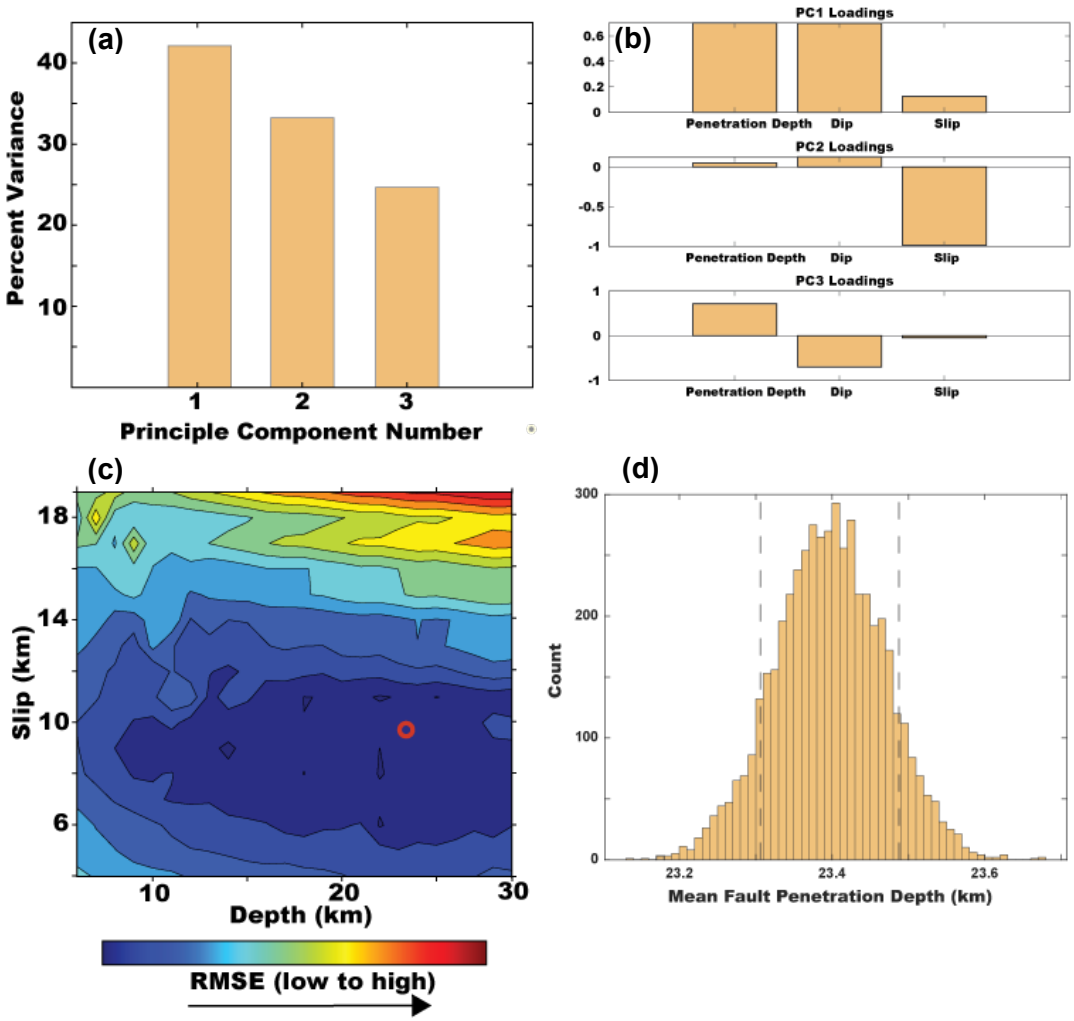

Figure C1. Principle component analysis (PCA) giving the percent variance between depth, slip amount, and dip angle of the for model solutions below 0.2 RMSE within profile 12 in Ridge ID 4 presented in **Figure 10** (**a**). Loadings for each principal component are given (**b**) and show that slip amount is responsible for the least variance within PC1. A contour map for the modeled parameter space detailing the response of model solutions to input parameters. This plot gives the root-mean-squared error (RMSE) in response to slip amount and fault penetration depth (**c**). Cool colors represent a lower RMSE, with the best solution highlighted by the red circle. Histogram for the distribution of bootstrapped mean values for modeled fault penetration depth for model solutions below 0.2 RMSE (**d**). Black dotted lines give the 90% confidence interval. This analysis yielded a mean penetration depth of 23.4 ± 0.09 km.

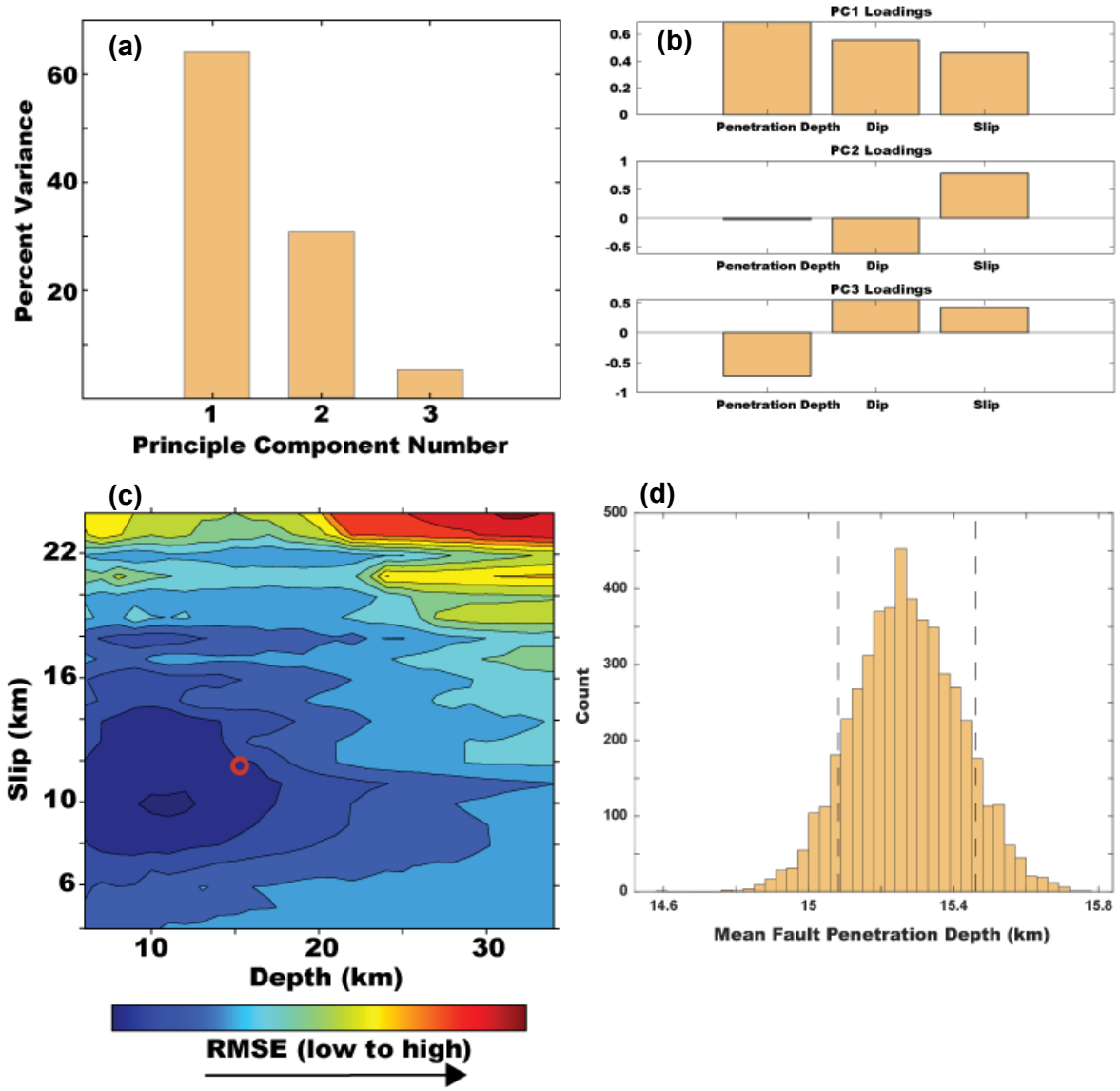

Figure C2. Principle component analysis (PCA) giving the percent variance between depth, slip amount, and dip angle of the for model solutions below 0.2 RMSE within profile 6 in Ridge ID 7 presented in **Figure 10** (**a**). Loadings for each principal component are given (**b**) and show that slip amount is responsible for the least variance within PC1. A contour map for the modeled parameter space detailing the response of model solutions to input parameters. This plot gives the root-mean-squared error (RMSE) in response to slip amount and fault penetration depth (**c**). Cool colors represent a lower RMSE, with the best solution highlighted by the red circle. Histogram for the distribution of bootstrapped mean values for modeled fault penetration depth for model solutions below 0.2 RMSE (**d**). Black dotted lines give the 90% confidence interval. This analysis yielded a mean penetration depth of 15.3 ± 0.15 km.

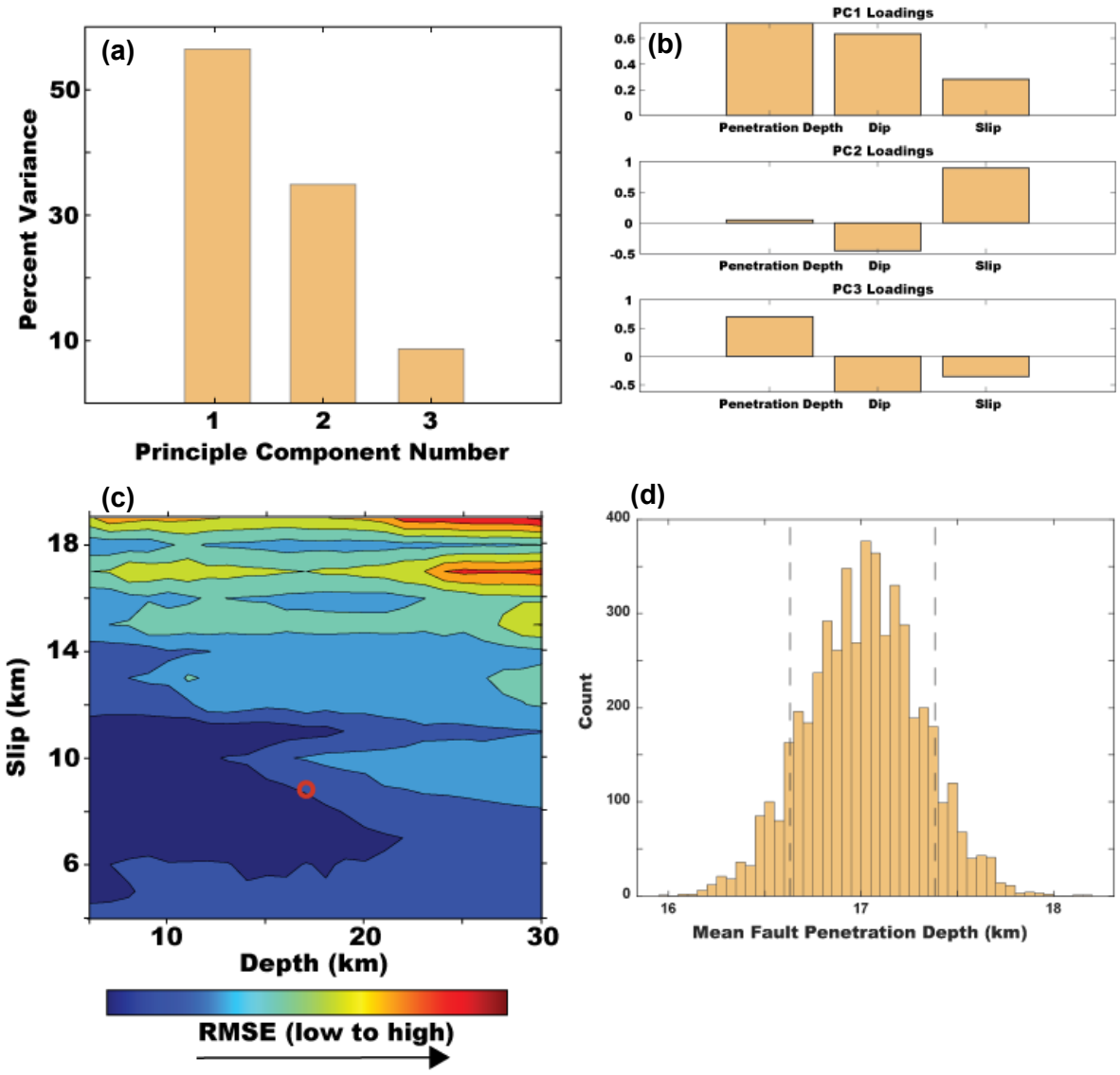

Figure C3. Principle component analysis (PCA) giving the percent variance between depth, slip amount, and dip angle of the for model solutions below 0.2 RMSE within profile 12 in Ridge ID 7 presented in **Figure 10** (**a**). Loadings for each principal component are given (**b**) and show that slip amount is responsible for the least variance within PC1. A contour map for the modeled parameter space detailing the response of model solutions to input parameters. This plot gives the root-mean-squared error (RMSE) in response to slip amount and fault penetration depth (**c**). Cool colors represent a lower RMSE, with the best solution highlighted by the red circle. Histogram for the distribution of bootstrapped mean values for modeled fault penetration depth for model solutions below 0.2 RMSE (**d**). Black dotted lines give the 90% confidence interval. This analysis yielded a mean penetration depth of 17.0 ± 0.38 km.

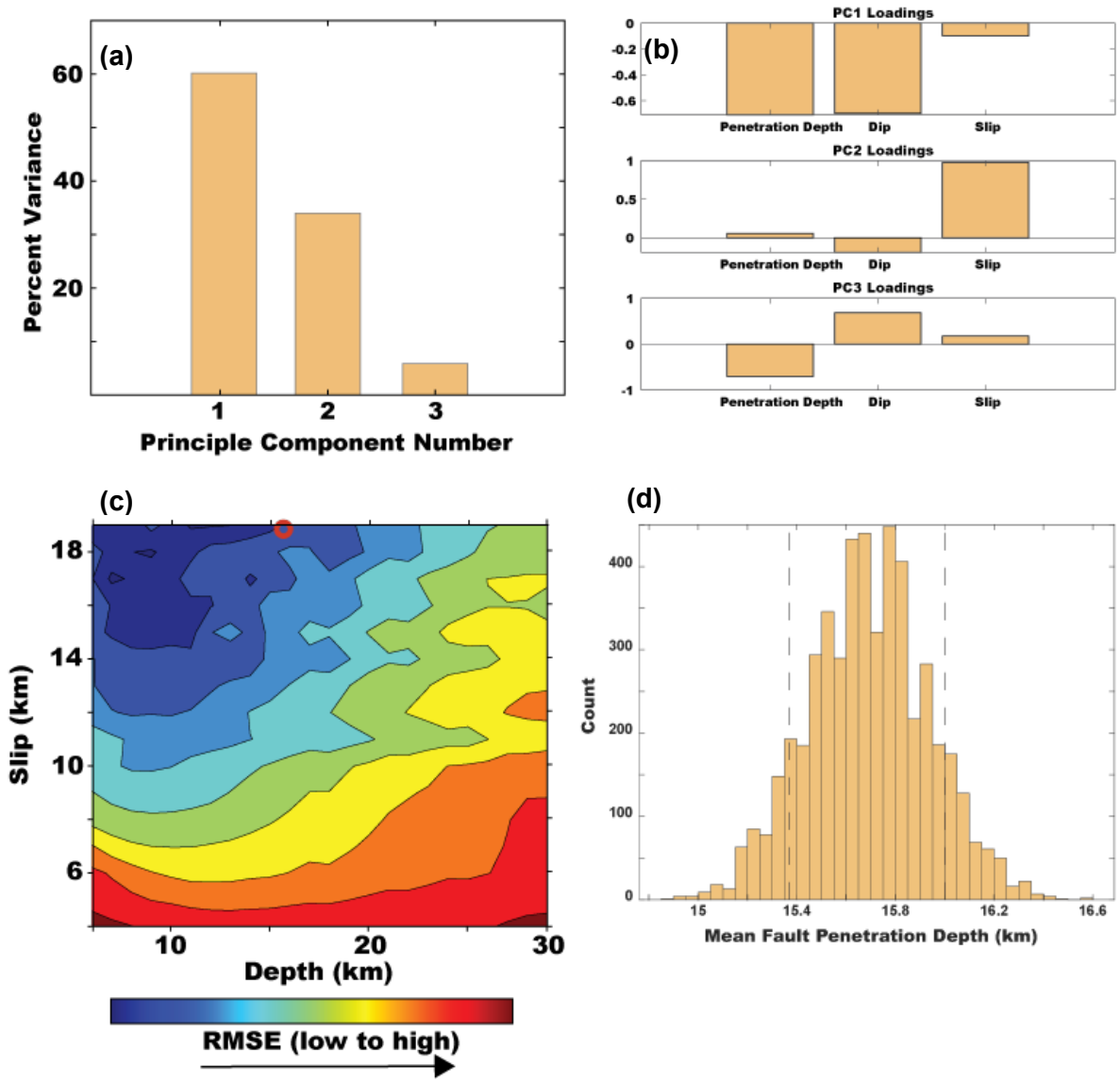

Figure C4. Principle component analysis (PCA) giving the percent variance between depth, slip amount, and dip angle of the for model solutions below 0.2 RMSE within profile 8 in Ridge ID 9 presented in **Figure 10** (**a**). Loadings for each principal component are given (**b**) and show that slip amount is responsible for the least variance within PC1. A contour map for the modeled parameter space detailing the response of model solutions to input parameters. This plot gives the root-mean-squared error (RMSE) in response to slip amount and fault penetration depth (**c**). Cool colors represent a lower RMSE, with the best solution highlighted by the red circle. Histogram for the distribution of bootstrapped mean values for modeled fault penetration depth for model solutions below 0.2 RMSE (**d**). Black dotted lines give the 90% confidence interval. This analysis yielded a mean penetration depth of 15.6 ± 0.4 km.

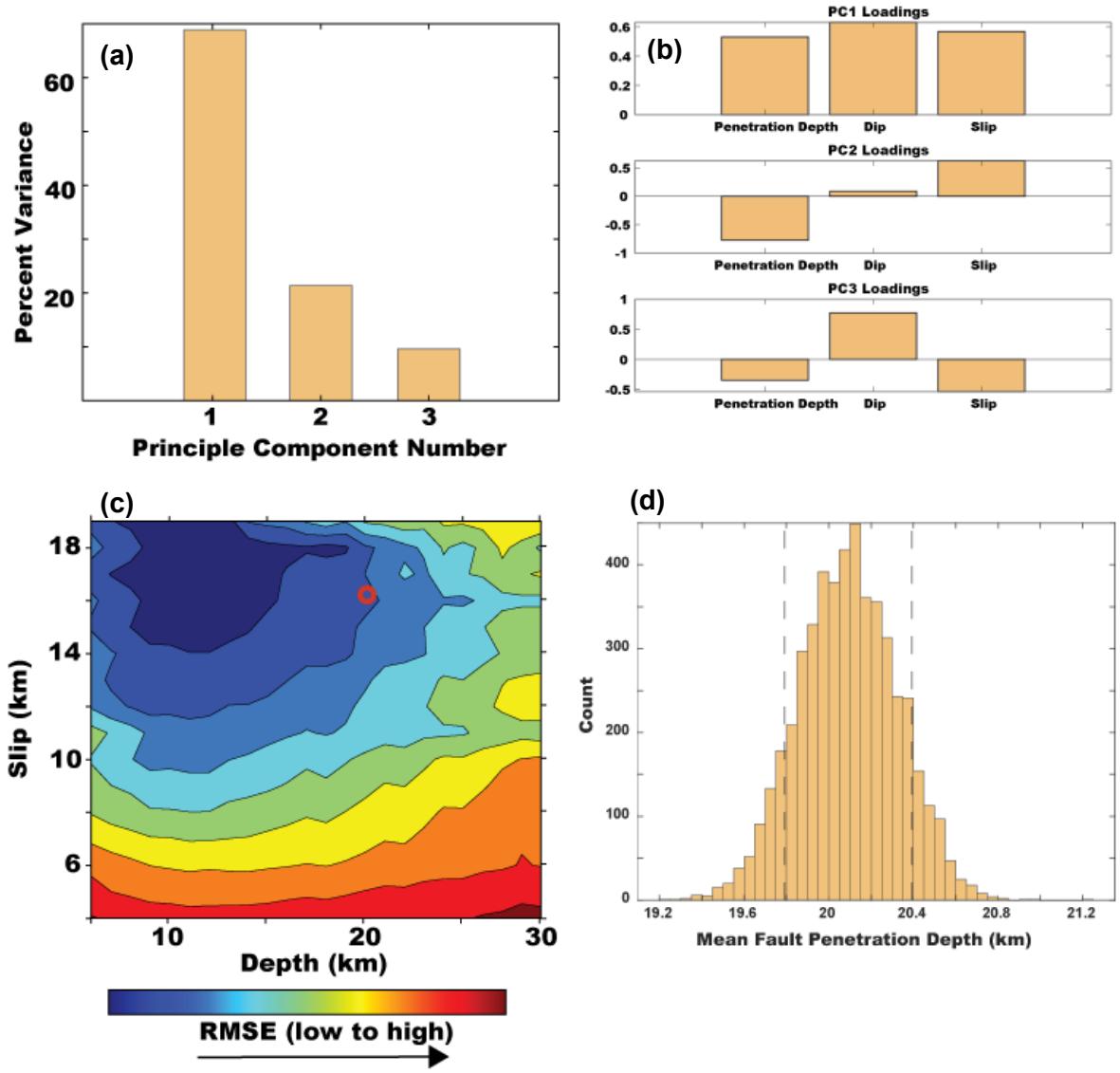

Figure C5. Principle component analysis (PCA) giving the percent variance between depth, slip amount, and dip angle of the for model solutions below 0.2 RMSE within profile 12 in Ridge ID 9 presented in **Figure 10** (**a**). Loadings for each principal component are given (**b**) and show that fault penetration depth is responsible for the least variance within PC1. A contour map for the modeled parameter space detailing the response of model solutions to input parameters. This plot gives the root-mean-squared error (RMSE) in response to slip amount and fault penetration depth (**c**). Cool colors represent a lower RMSE, with the best solution highlighted by the red circle. Histogram for the distribution of bootstrapped mean values for modeled fault penetration depth for model solutions below 0.2 RMSE (**d**). Black dotted lines give the 90% confidence interval. This analysis yielded a mean penetration depth of 20.1 ± 0.30 km.

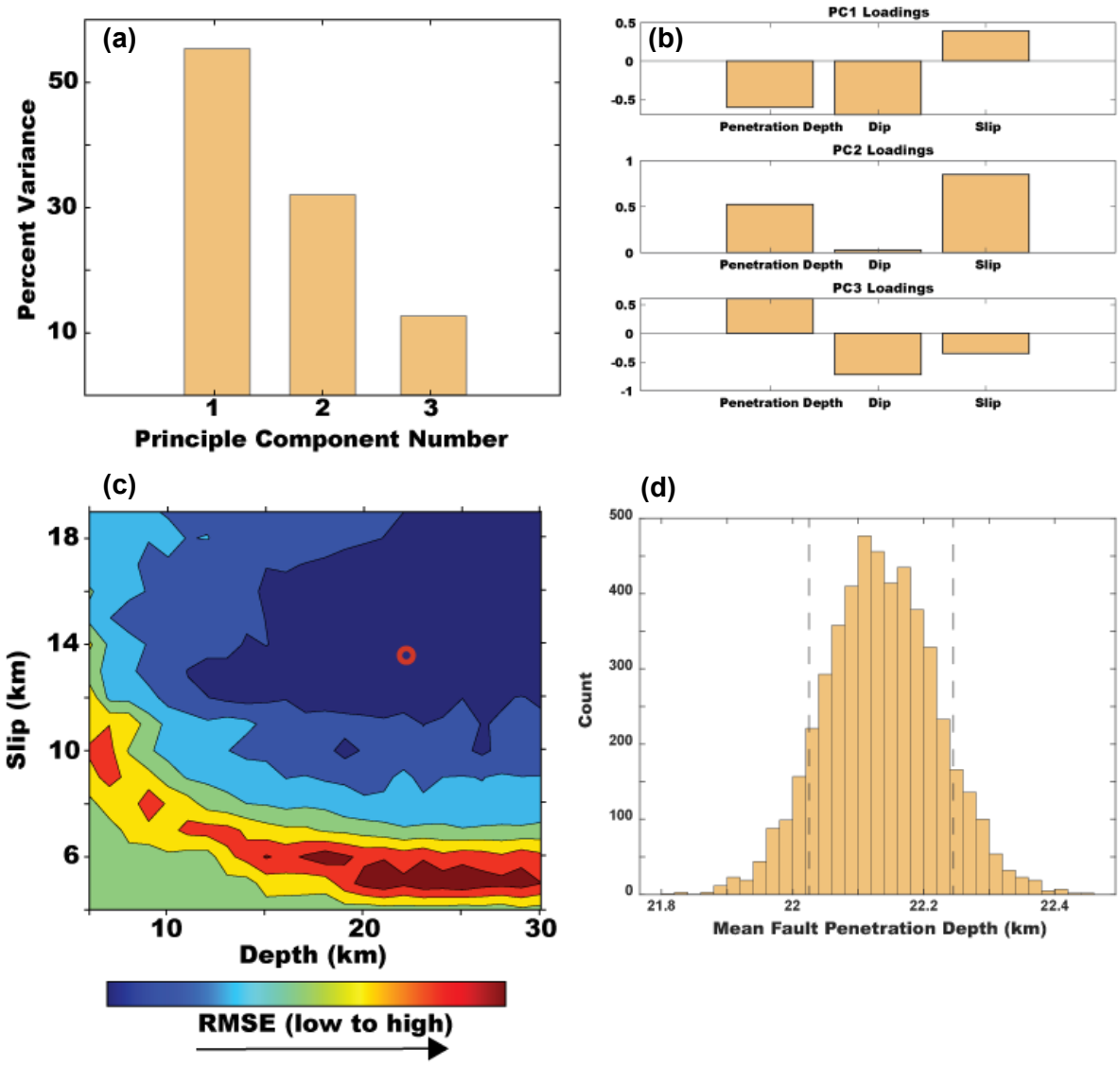

Figure C3. Principle component analysis (PCA) giving the percent variance between depth, slip amount, and dip angle of the for model solutions below 0.2 RMSE within profile 18 in Ridge ID 13 presented in **Figure 10** (**a**). Loadings for each principal component are given (**b**) and show that slip amount is responsible for the least variance within PC1. A contour map for the modeled parameter space detailing the response of model solutions to input parameters. This plot gives the root-mean-squared error (RMSE) in response to slip amount and fault penetration depth (**c**). Cool colors represent a lower RMSE, with the best solution highlighted by the red circle. Histogram for the distribution of bootstrapped mean values for modeled fault penetration depth for model solutions below 0.2 RMSE (**d**). Black dotted lines give the 90% confidence interval. This analysis yielded a mean penetration depth of 22.1 ± 0.10 km.